

**Implementation and assessment of a model including mixotrophs and the carbonate cycle (Eco3M\_MIX-CarbOx v1.0) in a highly dynamic Mediterranean coastal environment (Bay of Marseille, France) (Part. II): Towards a better representation of total alkalinity when modelling the carbonate system and air-sea CO<sub>2</sub> fluxes**

Lucille Barré<sup>1</sup>, Frédéric Diaz<sup>1,†</sup>, Thibaut Wagener<sup>1</sup>, Camille Mazoyer<sup>1</sup>, Christophe Yohia<sup>2</sup> and Christel Pinazo<sup>1</sup>

<sup>1</sup>Aix Marseille Univ., Université de Toulon, CNRS, IRD, MIO, UM 110, 13288, Marseille, France

<sup>2</sup>Aix Marseille Univ., Université de Toulon, CNRS, IRD, OSU Institut Pythéas, 13288, Marseille France

<sup>†</sup>Deceased

*Correspondence to:* Lucille Barré ([lucille.barre@mio.osupytheas.fr](mailto:lucille.barre@mio.osupytheas.fr)), Thibaut Wagener ([thibaut.wagener@mio.osupytheas.fr](mailto:thibaut.wagener@mio.osupytheas.fr))

## Abstract

The Bay of Marseille (BoM), located in the north-western Mediterranean Sea, is affected by various hydrodynamic processes (e.g., Rhône River intrusion and upwelling events) that result in a highly complex local carbonate system. In any complex environment, the use of models is advantageous since it allows to identify the different environmental forcings, thereby facilitating a better understanding. By combining approaches from two biogeochemical ocean models and improving the formulation of total alkalinity, we develop a more realistic representation of the carbonate system variables at high temporal resolution which enables us to study air-sea CO<sub>2</sub> fluxes and seawater pCO<sub>2</sub> variations more reliably. We apply this new formulation to two particular scenarios, typical for the BoM: (i) summer upwelling and (ii) Rhône River intrusion events. In both scenarios, our model was able to correctly reproduce the observed patterns of pCO<sub>2</sub> variability. Summer upwelling events are typically associated with pCO<sub>2</sub> decrease that mainly results from decreasing near-surface temperatures. Furthermore, Rhône River intrusion events are typically associated with pCO<sub>2</sub> decrease, although in this case the pCO<sub>2</sub> decrease results from a decrease in salinity and an overall increase in total alkalinity. While our model was able to correctly represent the daily range of air-sea CO<sub>2</sub> fluxes, we were unable to correctly estimate the yearly total air-sea CO<sub>2</sub> flux. Although the model is consistent with observations, it predicted the BoM to be a sink of CO<sub>2</sub> on a yearly basis, the magnitude of this CO<sub>2</sub> sink was underestimated which may be an indication of the limitations inherent in dimensionless models for representing air-sea CO<sub>2</sub> fluxes.

Keywords: Carbonate system, Bay of Marseille, Total alkalinity, Air-sea CO<sub>2</sub> fluxes, Modelling, Acidification

## 1 Introduction

Since the industrial revolution, atmospheric CO<sub>2</sub> concentrations have constantly increased (Mauna Loa Observatory: <https://gml.noaa.gov/ccgg/trends/>). By absorbing large amounts of CO<sub>2</sub>, the global ocean acts as an important sink of anthropogenic CO<sub>2</sub>. Recent estimates suggest that this absorption corresponds to roughly 25 % of annual emissions (Friedlingstein et al., 2022). During this absorption process, CO<sub>2</sub> undergoes a series of acid-base reactions that eventually lead to the formation of carbonate ions (CO<sub>3</sub><sup>2-</sup>). Initially, dissolved CO<sub>2</sub> reacts with water to form carbonic acid (H<sub>2</sub>CO<sub>3</sub>) which then, dissociates into bicarbonate (HCO<sub>3</sub><sup>-</sup>) and hydronium (H<sup>+</sup>) ions. In turn, HCO<sub>3</sub><sup>-</sup> dissociates into CO<sub>3</sub><sup>2-</sup> and H<sup>+</sup> ions. Increased uptake of atmospheric CO<sub>2</sub> modifies this acid-base reaction chain, thus affecting the associated species concentrations, particularly of H<sup>+</sup> ions which increase significantly resulting in a decrease in seawater pH. This phenomenon, known as ocean acidification (OA), is ubiquitous as confirmed through global observations (Feely et al., 2009; Dore et al., 2009; Gonzales-Dávila et al., 2010; Bates et al., 2012). The increased uptake of atmospheric CO<sub>2</sub> not only results in lower pH but also modifies the overall carbonate equilibrium which is slowly shifting toward higher HCO<sub>3</sub><sup>-</sup> and H<sub>2</sub>CO<sub>3</sub> concentrations and lower CO<sub>3</sub><sup>2-</sup> concentrations, which makes it more difficult for marine calcifiers to form their calcium carbonate shells (Orr et al., 2005).

Coastal oceans (depth < 200 m, Gattuso et al., 1998) accounts for over 10 % (0.18 to 0.45 PgC per year, Laruelle et al., 2010;

2014) of the total oceanic CO<sub>2</sub> uptake (Thomas et al., 2004) and are therefore particularly impacted by OA, generally exhibiting more pronounced localized decreases in pH (e.g., Kapsenberg et al., 2017; Luchetta et al., 2010). Nonetheless, coastal environments are highly complex mainly due to their high spatial and temporal variability, which makes their response to changes difficult to predict (Carstensen et al., 2018). Their proximity to the land means they are particularly exposed to anthropogenic pressures (run off and riverine input of anthropogenic nutrients and other chemical products, and organic matter rejects). Moreover, they are affected by strong physical forcings (e.g., tides, salinity gradients, wind induced currents) and account for about 30 % of all oceanic primary production which typically results in rich and diverse ecosystems (Gattuso et al., 1998).

The Mediterranean Sea is comparatively small and semi-enclosed; it receives nutrients through several pathways including Saharan dust depositions (Guerzoni et al., 1997) and numerous riverine inputs (e.g., Hopkins, 1992; Salat et al., 2002; Pujol-Pay et al., 2006). Considering that the Mediterranean Sea is mostly oligotrophic (Morel & Andre, 1991), these inputs are highly significant for phytoplankton growth (Revelante & Gillmartin, 1976; Ludwig et al., 2009). These features render the biogeochemistry of the Mediterranean Sea particularly complex, especially regarding the carbonate system. Several studies have investigated the carbonate system and air-sea CO<sub>2</sub> fluxes in these areas, typically using point measurements from various locations including, the Ligurian Sea (De Carlo et al., 2013; Kapsenberg et al., 2017), the Bay of Marseille (BoM; Wimart-Rousseau et al., 2020), the Gulf of Trieste (Ingrosso et al., 2016) and the Adriatic Sea (Urbini et al., 2020). Overall, these studies agree with findings by Roobaert et al. (2019) who showed that coastal systems mostly act like CO<sub>2</sub> sinks on a yearly basis, although the CO<sub>2</sub> uptake shows a significant intra-annual variability.

Most modelling approaches to investigate carbonate system variables typically employ 3D coupled physical-biogeochemical models and focus on larger coastal areas (e.g., Artioli et al., 2014; Bourgeois et al., 2016). If the focus is on smaller areas this requires higher spatial and temporal resolution to correctly represent the relevant processes (Bourgeois et al., 2016).

However, higher spatial and temporal resolution often result in a significant increase of the calculation time which make more difficult the repetition of numerical experiments, an important step to better understanding the global functioning of the area and its reaction to environmental forcings. A solution to avoid important calculation times is to use a dimensionless model. This type of model allows to conduct large amount of test in short amount of time. For instance, Lajaunie-Salla et al. (2021) used the dimensionless Eco3M-CarbOx model, which contains a carbonate module performing the resolution of the carbonate system based on total alkalinity (TA) and dissolved inorganic carbon (DIC). Even if the DIC, oceanic partial pressure of CO<sub>2</sub> ( $p\text{CO}_2$ ) and total pH ( $\text{pH}_T$ ) representations look reliable, Eco3m-CarbOx tends to minimize the range of TA variations during the year, resulting in a near constant TA (Lajaunie-Salla et al., 2021).

Here we try to provide a more realistic representation of carbonate system variables in the BoM. As a starting point, we used the concept of the dimensionless Eco3M-CarbOx model (Lajaunie-Salla et al., 2021), which aims to represent a small volume of surface water (i.e., 1 m<sup>3</sup>) in the BoM. We developed a planktonic ecosystem model which contains, among others, mixotrophic organisms, modified the carbonate module described by Lajaunie-Salla et al. (2021) and added it to our newly developed planktonic ecosystem model to obtain the Eco3M\_MIX-CarbOx model (v1.0). We implemented two types of TA

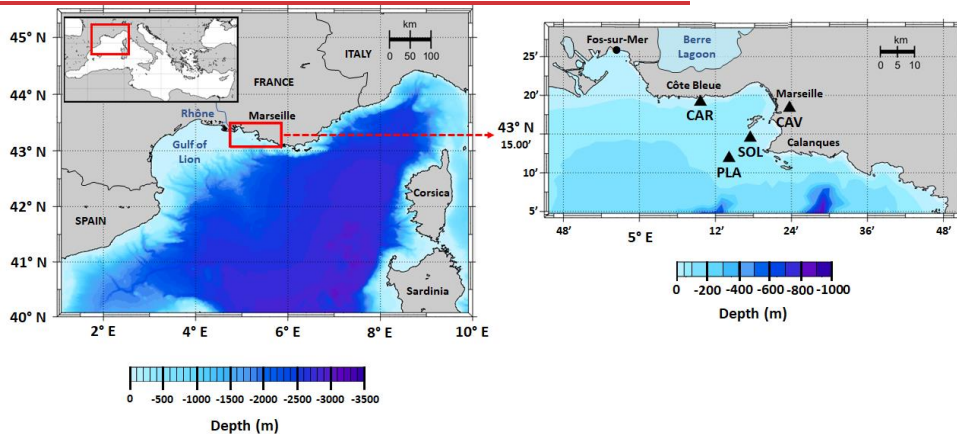
a mis en forme : Anglais (Royaume-Uni)

formulation and compared the simulation results to in situ observations to identify which formulation was capable of deliver the more realistic results: (i) a formulation that only considers biological processes (referred to as autochthonous formulation) and (ii) a new TA formulation that depends only on salinity (referred to as allochthonous formulation).  
 80 Furthermore, we simulate air-sea CO<sub>2</sub> fluxes to determine whether the BoM act as a sink or a source of CO<sub>2</sub> and provide a detailed analysis of drivers of seawater pCO<sub>2</sub> variations for two specific hydrodynamic processes typical for the BoM: (i) Rhône River intrusion and (ii) summer upwelling events. With this study, we aim to provide a new tool which allow to obtain a reliable representation of the carbonate system in the simplest way as possible: by using a dimensionless configuration which is easy to use, adapt and give results in a short amount of time.

85 Eco3M\_MIX-CarbOx model contains both a mixotrophy compartment and a representation of the carbonate system. The model description is split in two parts: (i) a description of how the organisms and their dynamics are represented in the model, with a particular focus on mixotrophic organisms, and (ii) a more detailed description of the carbonate module and the associated dynamics. While (ii) is presented here, (i) has been presented in a companion paper (Barré et al., 2023a).

## 90 2 Materials and methods

### 2.1 Study area



95 **Figure 1.** Map of the study area showing the location of SOLEMIO station (SOL: 43°14.30' N, 5°17.30' E), Planier station (PLA: 43°11.96' N, 5°14.07' E), Carry-buoy (CAR: 43°19.15' N, 5°09.64' E) and Cinq Avenue station (CAV: 43°18.40' N, 5°23.70' E) (based on Barré et al., 2023a; modified).

The BoM is located in the NW Mediterranean Sea, in the eastern part of the Gulf of Lion near Marseille (Fig. 1). Due to its proximity to Marseille, the second biggest city in France, and to other urbanized areas along the coast (e.g., Fos-sur-Mer and

Berre Lagoon to the west, Fig. 1), the BoM is strongly affected by anthropogenic forcings which results in significant inputs of anthropogenic nutrients as ammonia and phosphate, chemical products, and organic matter (Millet et al., 2018) through urban rivers. Significant quantities of nutrients and freshwater are also provided by the Rhône River (Pont et al., 2002) of which the delta is located 35 km to the west of the bay. In specific wind conditions, Rhône River plume can be pushed eastwards, supplying the bay with nitrate which tend to boost the productivity of the area (Gatti et al., 2006; Fraysse et al., 2013, 2014). In addition to these inputs, the biogeochemical functioning of the BoM is affected by various hydrodynamic processes including strong Mistral events (Yohia, 2017), upwelling events (Millot, 1990) which generally take place in specific locations: the Calanques of Marseille and the Côte Bleue (Fig. 1), development of eddies (Schaeffer et al., 2011) and intrusions of oligotrophic water masses via the Northern Current (Barrier et al., 2016; Ross et al., 2016).

In Eco3M\_MIX-CarbOx, environmental forcings are provided by in situ measurements of sea surface temperature (referred as temperature in the following), salinity and atmospheric  $p\text{CO}_2$  in combination with simulation data of wind speed and solar irradiance. Environmental forcings has already been described in detail in Barré et al. (2023a), their main characteristics are reminded in Table 1.

**Table 1. Data types and their sources used to drive the environmental forcing during the 2017 model run (based on Barré et al., 2023a).**

	Data type	Location	Time resolution
<b>Sea surface temperature</b>	Measurements	Planier station	Hourly
<b>Salinity</b>	Measurements	Carry buoy	Hourly
<b>Wind</b>	WRF model results	SOLEMIO station	Hourly
<b>Irradiance</b>	WRF model results	SOLEMIO station	Hourly
<b>Atmospheric <math>p\text{CO}_2</math></b>	Measurements	Cinq Avenues station	Hourly

a mis en forme le tableau

To evaluate our representation of carbonate system variables, we compared our model results to in situ measurements by using a carbonate parameters data set which includes TA, DIC, pH,  $p\text{CO}_2$  and salinity data (<https://www.seanoe.org>, last access: 14 February 2023). Measurements are performed fortnightly at SOLEMIO station.

A map of the study area showing the location of stations where measurements were carried, and places of interest can be found in Barré et al. (2023a).

## 2.2 Model description

In this study, we used the Eco3M\_MIX-CarbOx model (v1.0) which was developed to represent the dynamics of the seawater carbonate system and mixotrophs in the BoM and was implemented using the Eco3M (Ecological Mechanistic and Molecular Modelling) platform (Baklouti et al., 2006a, b). Eco3M\_MIX-CarbOx is a dimensionless model (0D): we consider a volume of  $1 \text{ m}^3$  of surface water at SOLEMIO station, in this volume the state variables only vary over time as the model is not coupled with a hydrodynamic model. We chose to use a 0D configuration as this configuration has several

a mis en forme : Exposant

125 advantages namely, calculation times are low (around 45 minutes in our case). It allows to make several test simulations to  
 130 better understand the biogeochemical functioning of the BoM and its possible reactions to environmental forcings. In the  
 following, we provide a detailed description of the carbonate system module. We also give a brief description of nutrients  
and organic matter representation. A detailed description of other compartments, especially of mixotrophs compartment can  
 be found in Barré et al. (2023a). Equations and parameters used by the model are also explained in this previous study. The  
 Eco3M\_MIX-CarbOx model includes seven compartments: zooplankton, mixotrophs, phytoplankton, heterotrophic bacteria,  
 135 labile dissolved organic matter, detritic particulate organic matter, and dissolved inorganic matter with the following  
 carbonate system variables: dissolved inorganic carbon (DIC), total alkalinity (TA), pH calculated on total scale (pH<sub>T</sub>), and  
 oceanic partial pressure of CO<sub>2</sub>: (pCO<sub>2</sub>). The carbonate system resolution required knowledge of at least two from among the  
 four main variables of TA, DIC, pH<sub>T</sub> and pCO<sub>2</sub>. As TA and DIC are conserved, a requirement to solve the source-sinks state  
 equations, we used those variables to perform the system resolution. To provide a more realistic representation of the  
 140 carbonate system, we modified the carbonate module described by Lajaunie-Salla et al. (2021) by focusing mainly on the  
 state equations of TA and DIC, as a realistic implementation of TA and DIC state variables is crucial to obtain reliable  
 estimates of the diagnostic variables pH<sub>T</sub>, and pCO<sub>2</sub>. In addition to a modified carbonate module, Eco3M\_MIX-CarbOx  
 contains a mixotroph compartment which is crucial for a reliable representation of TA and DIC, as the presence of  
 mixotrophs affects total photosynthesis, total respiration, as well as uptake and precipitation fluxes (Mitra et al. 2014).

### 140 2.2.1 Nutrients and organic matter representation

As we use a dimensionless configuration, we assume that nutrients are fully the result of autochthonous biological processes.  
In other terms, we do not consider allochthonous inputs of nutrients (i.e., from rivers or atmosphere as instance). For all the  
simulations, nutrients dynamics are represented by the following state equations:

$$\frac{\partial \text{NO}_3}{\partial t} = \text{Nitrif}_{\text{NO}_3}^{\text{NH}_4} - \sum_{i=1}^2 \left( \text{Upt}_{\text{NO}_3}^{\text{PhyN}_i} \right) - \text{Upt}_{\text{NO}_3}^{\text{CMN}_i}$$

$$145 \frac{\partial \text{NH}_4}{\partial t} = \text{Excr}_{\text{NH}_4}^{\text{COPN}} + \text{Excr}_{\text{NH}_4}^{\text{NCMN}} + \text{Remin}_{\text{NH}_4}^{\text{BACN}} - \sum_{i=1}^2 \left( \text{Upt}_{\text{NH}_4}^{\text{PhyN}_i} \right) - \text{Upt}_{\text{NH}_4}^{\text{CMN}} - \text{Upt}_{\text{NH}_4}^{\text{BACN}} - \text{Nitrif}_{\text{NH}_4}^{\text{NO}_3}$$

$$\frac{\partial \text{PO}_4}{\partial t} = \text{Excr}_{\text{PO}_4}^{\text{COPP}} + \text{Excr}_{\text{PO}_4}^{\text{NCMP}} + \text{Remin}_{\text{PO}_4}^{\text{BACP}} - \sum_{i=1}^2 \left( \text{Upt}_{\text{PO}_4}^{\text{PhyP}_i} \right) - \text{Upt}_{\text{PO}_4}^{\text{CMP}} - \text{Upt}_{\text{PO}_4}^{\text{BACP}}$$

(1)

150 The NO<sub>3</sub><sup>-</sup> concentration results from nitrification and phytoplankton and CM uptakes. NH<sub>4</sub><sup>+</sup> concentration results from  
copepods and NCM excretion, remineralisation by heterotrophic bacteria, heterotrophic bacteria, phytoplankton, and CM  
uptakes and losses from nitrification. PO<sub>4</sub><sup>3-</sup> concentration results from copepods and NCM excretion, remineralisation by  
heterotrophic bacteria and heterotrophic bacteria, phytoplankton, and CM uptakes.

a mis en forme : Titre 3

a mis en forme : Police :Times New Roman, Non Italique

a mis en forme : Police :Times New Roman, Non Italique

a mis en forme : Indice

a mis en forme : Exposant

a mis en forme : Indice

a mis en forme : Exposant

a mis en forme : Indice

a mis en forme : Exposant

Such as nutrients dynamics, organic matter (OM, dissolved and particulate) dynamic is only the result of autochthonous biological processes (Eq. 2 and 3).

$$\frac{\partial \text{DOC}}{\partial t} = \sum_{i=1}^2 (\text{Exu}_{\text{DOC}}^{\text{PHY}_{Ci}}) + \sum_{i=1}^2 (\text{Exu}_{\text{DOC}}^{\text{MIX}_{Ci}}) + \text{Excr}_{\text{DOC}}^{\text{COP}_C} + \text{Mort}_{\text{DOC}}^{\text{BAC}_C} - \text{BP}_{\text{DOC}}^{\text{BAC}_C}$$

a mis en forme : Police :Times New Roman, Non Italique

$$\frac{\partial \text{DON}}{\partial t} = \sum_{i=1}^2 (\text{Exu}_{\text{DON}}^{\text{PHY}_{Ni}}) + \sum_{i=1}^2 (\text{Exu}_{\text{DON}}^{\text{MIX}_{Ni}}) + \text{Mort}_{\text{DON}}^{\text{BAC}_N} - \text{Upt}_{\text{DON}}^{\text{CM}_N} - \text{Upt}_{\text{DON}}^{\text{PICO}_N} - \text{Upt}_{\text{DON}}^{\text{BAC}_N}$$

a mis en forme : Police :Times New Roman, Non Italique

$$\frac{\partial \text{DOP}}{\partial t} = \sum_{i=1}^2 (\text{Exu}_{\text{DOP}}^{\text{PHY}_{Pi}}) + \sum_{i=1}^2 (\text{Exu}_{\text{DOP}}^{\text{MIX}_{Pi}}) + \text{Mort}_{\text{DOP}}^{\text{BAC}_P} - \text{Upt}_{\text{DOP}}^{\text{CM}_P} - \text{Upt}_{\text{DOP}}^{\text{PICO}_P} - \text{Upt}_{\text{DOP}}^{\text{BAC}_P}$$

a mis en forme : Police :Times New Roman, Non Italique

(2)

The concentration of dissolved organic (DOC), nitrogen (DON) and phosphorus (DOP) depends on phytoplankton and mixotrophs exudation, copepods excretion (DOC only), heterotrophic bacteria mortality (natural mortality) and CM, PICO and heterotrophic bacteria uptake.

$$\frac{\partial \text{POC}}{\partial t} = \text{E}_{\text{POC}}^{\text{COP}_C} + \text{Predation}_{\text{POC}}^{\text{COP}_C} - \text{BP}_{\text{POC}}^{\text{BAC}_C}$$

$$\frac{\partial \text{PON}}{\partial t} = \text{E}_{\text{PON}}^{\text{COP}_N} + \text{Predation}_{\text{PON}}^{\text{COP}_N} - \text{Upt}_{\text{PON}}^{\text{BAC}_N}$$

a mis en forme : Police :Times New Roman, Non Italique

$$\frac{\partial \text{POP}}{\partial t} = \text{E}_{\text{POP}}^{\text{COP}_P} + \text{Predation}_{\text{POP}}^{\text{COP}_P} - \text{Upt}_{\text{POP}}^{\text{BAC}_P}$$

(3)

a mis en forme : Droite

The concentration of particulate organic carbon (POC), nitrogen (PON), and phosphorus (POP) depends on copepods egestion, predation by higher trophic levels on copepods (closure terms of the model) and heterotrophic bacteria production and uptake. POM particles are large enough to sink, however, we do not consider a term to represent their removal from the surface box by sinking. In our case, the POM, such as the DOM and nutrients, stay in the box and is constantly recycling. A detailed description and formulations of processes can be found in Barré et al. (2023a). Processes notation description can be found in Table A1 (Appendix A).

## 2.2.12 TA formulation

In Eco3m-CarbOx, TA representation lack variations during the year. Eco3m-CarbOx did not account for TA inputs by rivers, especially by the Rhône River which has an average alkalinity of 2885  $\mu\text{mol kg}^{-1}$  (Schneider et al., 2007). To remedy this shortcoming, we decided to express TA in two ways. In the first one, we considered only autochthonous TA variations.

In the second one, we considered allochthonous TA variations. We then compared the outputs from each formulation to in situ data to determine which formulation delivered the more realistic results.

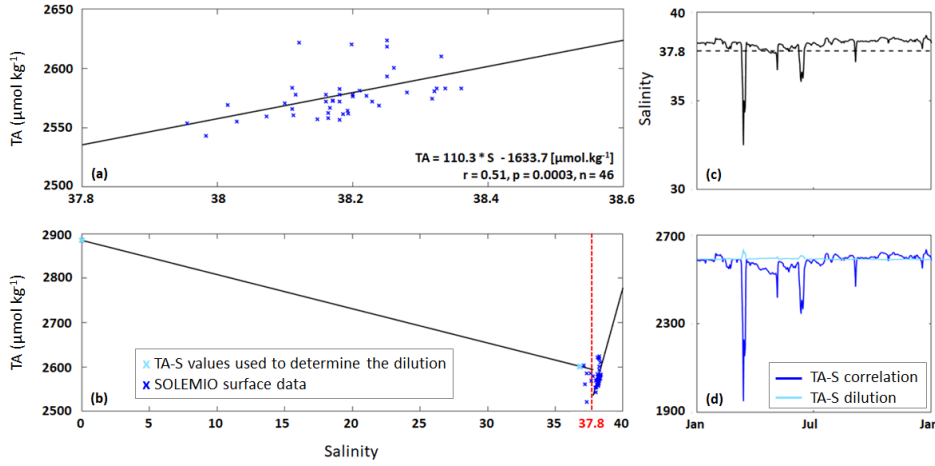


**Figure 12.** (a) TA-S correlation (black line) based on SOLEMIO surface data excluding low salinities  $\leq 37.8$  (b) TA-S dilution (for  $S \leq 37.8$ ) and TA-S correlation (for  $S > 37.8$ ) (c) Salinity data used by the model (solid line) and  $S = 37.8$  (dashed line) (d) TA calculated from TA-S correlation (Eq. 52) and TA-S dilution (Eq. 63).

For the autochthonous formulation, we relied on the Eco3M-CarbOx TA state equation which we modified to fit our modelled planktonic ecosystem. We first added a term of phosphate remineralisation by heterotrophic bacteria. By considering that the uptake of one mole of phosphate by phytoplankton increases TA by one mole, and vice versa, for one mole of phosphate released during remineralisation, TA decreases by one mole (Wolf-Gladrow et al., 2007a). As a last term we included the mixotrophic uptake of nutrients. **TA is calculated as follows, which yields the following state equation for TA:**

$$\frac{\partial TA}{\partial t} = 2 \cdot Dis_{TA}^{CaCO_3} + \sum_{i=1}^2 (Upt_{NO_3}^{PHY N_i}) + Upt_{NO_3}^{CM N} + \sum_{i=1}^2 (Upt_{PO_4}^{PHY P_i}) + Upt_{PO_4}^{CM P} + Remin_{NH_4}^{BAC N} - \sum_{i=1}^2 (Upt_{NH_4}^{PHY N_i}) - Upt_{NH_4}^{CM N} - Remin_{PO_4}^{BAC P} - 2 \cdot Prec_{TA}^{CaCO_3} - 2 \cdot Nitrif_{TA}, \quad (4)$$

where  $i$  represents the number of organisms. **Processes description can be found in Table A1 (Appendix A) and formulations are available in Barré et al. (2023a).** In this formulation, TA only depends on biogeochemical processes (i.e., TA riverine inputs are excluded).

For the allochthonous formulation, we first determined an oceanic TA-S correlation (Eq. 52; Fig. 12a) using the measurements of carbonate system parameters at SOLEMIO station (see Sect. 2.1). We only considered the TA values

a mis en forme : Droite



195 associated to salinity values  $> 37.8$  as  $37.8$  was used as a threshold value to identify low salinity events (LSE), associated to Rhone River plume intrusions in the BoM (Fraysse et al 2014).

$$TA = 110.3 * S - 1633.7 \text{ (}\mu\text{mol kg}^{-1}\text{)}$$

a mis en forme : Exposant

(25)

a mis en forme : Droite

200 where TA has units of  $\mu\text{mol kg}^{-1}$ . Second, using only those TA values associated with LSE, we determined a separate TA-S formulation to quantify river water dilution (Eq. 63; Fig. 12b).

$$TA = -7.7 * S + 2885 \text{ (}\mu\text{mol kg}^{-1}\text{)}$$

a mis en forme : Exposant

(36)

a mis en forme : Droite

205 where TA is again in units of  $\mu\text{mol kg}^{-1}$ . The carbonate data set did not contain sufficient LSE data to create a reliable TA-S fit. Eq. (36) was therefore derived based on two TA-S data pairs: TA = 2885.0  $\mu\text{mol kg}^{-1}$  and S = 0, representative of water masses near Rhône River mouth (Schneider et al., 2007), and TA = 2600.6  $\mu\text{mol kg}^{-1}$  and S = 36.82, recorded at SOLEMIO station during a major LSE on March 15, 2017. Unlike Eq. (25), the TA-S dilution shows a negative slope typical of low salinity river water (Fig. 12b).

210 We implemented both TA-S formulations in our Eco3M\_MIX-CarbOx model, and the formulation to be used was chosen based on the salinity : if salinity value used by the model for the time step considered  $\leq 37.8$ , the TA-S dilution (Eq.36) was applied; else for salinity value  $> 37.8$  the TA-S correlation was applied (Eq. 5, Fig. 12c,d). With this method, TA only depends on salinity (i.e., biological processes are neglected).

### 2.2.23 DIC formulation

215 The DIC formulation used in our Eco3M\_MIX-CarbOx model is very similar to the formulation used in Eco3M-CarbOx except that we added the mixotroph organisms' processes to our equation. As a results, DIC depends on phytoplankton, mixotrophs, zooplankton and bacterial respiration, air-sea  $\text{CO}_2$  fluxes (aeration process), dissolution of  $\text{CaCO}_3$ , phytoplankton and mixotrophs photosynthesis and precipitation of  $\text{CaCO}_3$  (Eq.74).

$$\frac{\partial \text{DIC}}{\partial t} = \sum_{i=1}^2 \left( \text{Resp}_{\text{DIC}}^{\text{PHY}c_i} \right) + \sum_{i=1}^2 \left( \text{Resp}_{\text{DIC}}^{\text{MIX}c_i} \right) + \text{Resp}_{\text{DIC}}^{\text{COP2}\theta c} + \text{BR}_{\text{DIC}}^{\text{BAC}c} + \text{Aera}_{\text{DIC}} + \text{Diss}_{\text{DIC}}^{\text{CaCO}_3} - \sum_{i=1}^2 \left( \text{Photo}_{\text{DIC}}^{\text{PHY}c_i} \right) -$$

$$220 \sum_{i=1}^2 \left( \text{Photo}_{\text{DIC}}^{\text{MIX}c_i} \right) - \text{Prec}_{\text{DIC}}^{\text{CaCO}_3} - \text{Aera}_{\text{DIC}} ,$$

(47)

a mis en forme : Droite

where  $i$  represents the number of organisms. [Processes description can be found in Table A1 \(Appendix A\) and formulations are available in Barré et al. \(2023a\)](#). As an additional modification, we use a more recent version of the gas transfer velocity calculation introduced by Wanninkhof (2014). The air-sea CO<sub>2</sub> fluxes are determined according to :

$$A_{era} = \frac{K_{ex}}{H} * \alpha * (pCO_{2,sw} - pCO_{2,atm}),$$

(58)

a mis en forme : Droite

where  $A_{era}$  is in mmol m<sup>-3</sup> s<sup>-1</sup>.  $K_{ex}$  represents the gas transfer velocity (Wanninkhof, 2014) in cm h<sup>-1</sup>,  $\alpha$  the CO<sub>2</sub> solubility coefficient (Weiss, 1974) in mol L<sup>-1</sup> atm<sup>-1</sup>,  $pCO_{2,sw}$  the seawater  $pCO_2$  modelled at the previous time step in  $\mu$ atm,  $pCO_{2,atm}$  the atmospheric  $pCO_2$  from CAV in  $\mu$ atm and  $H$  the magnitude of the impacted layer in meters (in Eco3M\_MIX-CarbOx,  $H = 1$  m).  $K_{ex}$  is calculated using :

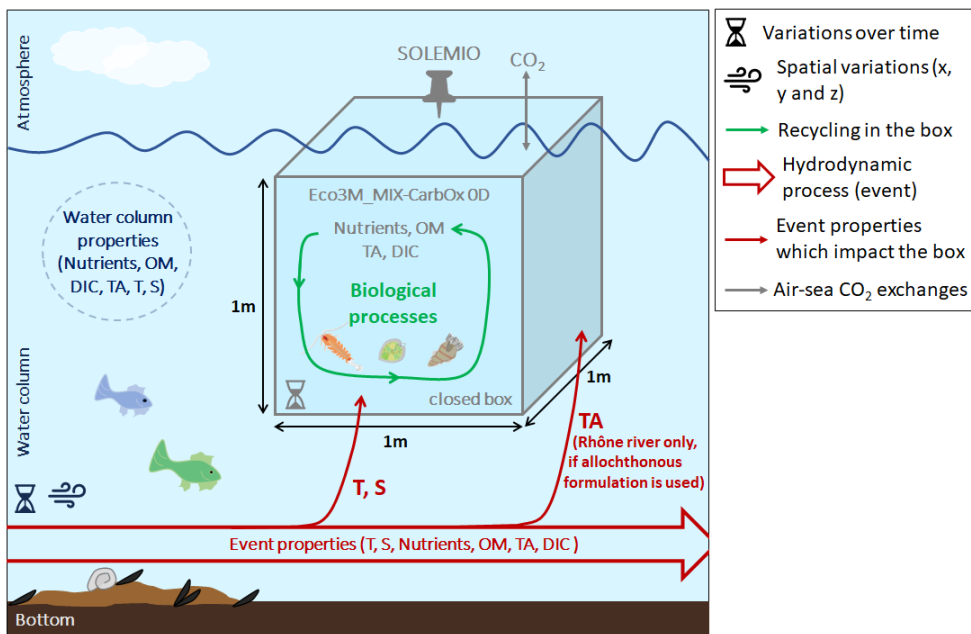
$$K_{ex} = 0.251 * U_{10}^2 * \left(\frac{660}{Sc}\right)^{\left(\frac{1}{2}\right)},$$

(69)

a mis en forme : Droite

where  $U_{10}$  is the wind speed in m s<sup>-1</sup> and  $Sc$  the Schmidt number calculated with the coefficients from Wanninkhof (2014). By convention, we will consider negative aeration values (i.e.,  $pCO_{2,atm} > pCO_{2,sw}$ ) to represent fluxes from the atmosphere into the ocean and vice versa. Furthermore, we will express air-sea CO<sub>2</sub> fluxes in the more frequently used units of mmol m<sup>-2</sup> per unit time.

[Figure 2 illustrates the concept of OD and summarizes the hypothesis used in this study with Eco3M\\_MIX-CarbOx.](#)



240 **Figure 2. Schematic representation of 0D concept and summary of hypotheses used in this study with Eco3M MIX-CarbOx. T: temperature, S: Salinity and OM: Organic matter.**

a mis en forme : Légende

### 2.2.34 pH<sub>T</sub> and pCO<sub>2</sub> calculation

Solving the equations of the carbonate system requires knowledge of TA and DIC. Depending on the TA formulation used, the steps followed by the model to issue the new pH<sub>T</sub> and pCO<sub>2</sub> are described on Fig. 3.

245 If TA is calculated using the Eq. (44), biogeochemical and aeration processes are applied as described in Eqs. (44) and (74) in order to deliver new ([t] time step) TA and DIC : Air-sea CO<sub>2</sub> fluxes are calculated from temperature, salinity, wind speed, atmospheric pCO<sub>2</sub> and seawater pCO<sub>2</sub>, and biogeochemical processes required, at least, temperature to be computed and solar irradiance. When calculated, processes are applied in the form of fluxes to the previous TA and DIC ([t-1] time step values) to solve their respective state equation. The pH<sub>T</sub> and pCO<sub>2</sub> calculation is, then, performed using in addition to

250 TA and DIC, temperature and salinity data. pH<sub>T</sub> is calculating using a buffering value (B) defined as the pH variation induced by an addition of acid or base to a specific DIC solution (Van Slycke, 1922). In seawater, B can be expressed in terms of TA (Middelburg, 2019) which yields:

$$B = \frac{\partial TA}{\partial pH_T} \Leftrightarrow \Delta pH_T = \frac{\partial TA}{\sum_{i=1}^n B_i}$$

255 where  $i$  represents a chemical species contributing to TA.  $pCO_2$  is obtained using:

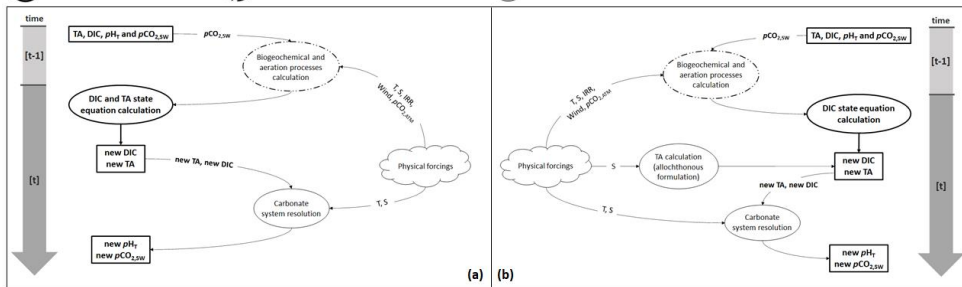
$$pCO_2 = \frac{DIC * [H^+]^2}{[H^+]^2 + K_1 + [H^+] + K_1 * K_2} * \frac{10^6}{K_0 * FugFac}$$

where  $pCO_2$  is in  $\mu atm$  and FugFac represents the fugacity factor. A more detailed description of the calculation is provided in Appendix B. At the end of the time step, TA, DIC,  $pH_T$  and  $pCO_2$  are written to file (Fig. 3a).

(710) a mis en forme : Droite

(811) a mis en forme : Droite

State variables calculation    State variables process calculation    Others calculations



260

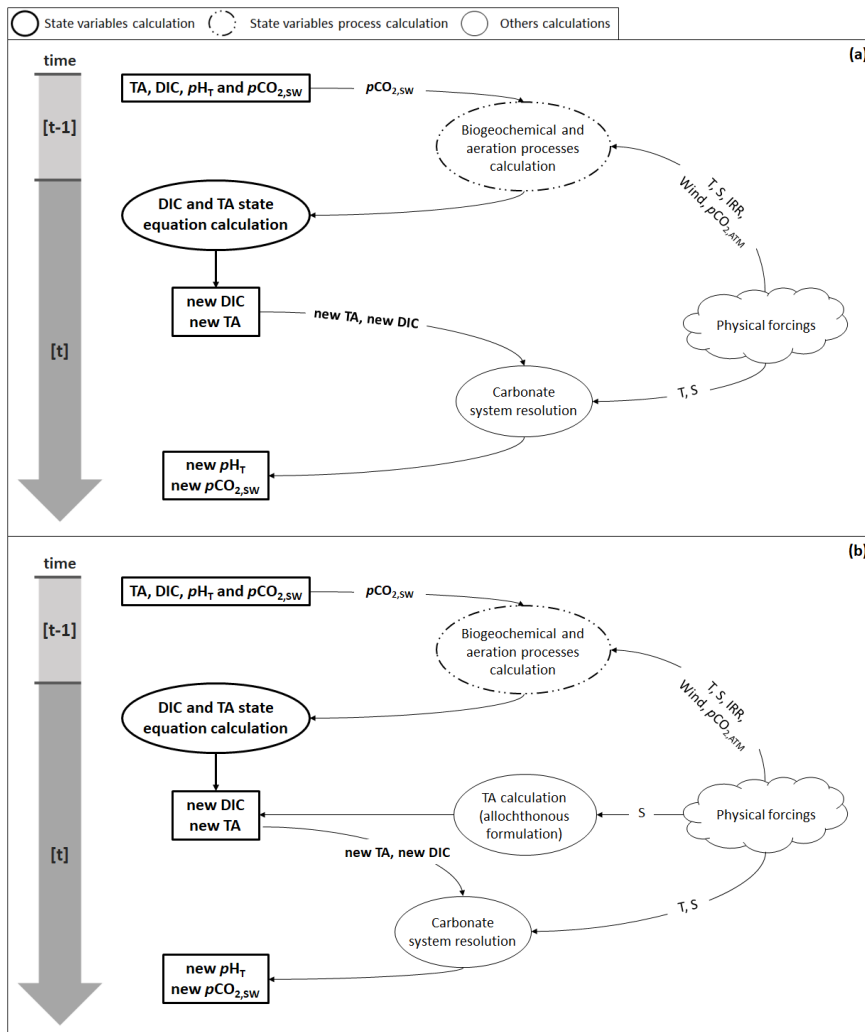


Figure 3. Flow diagram illustrating the steps needed to calculate  $pH_T$  and  $pCO_2$  (a) using the autochthonous formulation (Eq. 41) and (b) with the allochthonous formulation (Eq. 52 and 63). Physical forcings include temperature (T), salinity (S), solar irradiance (IRR), wind speed (Wind) and atmospheric  $pCO_2$  ( $pCO_{2,ATM}$ ).

a mis en forme : Centré

265 When TA is calculated using Eqs. (25) and (36), the biogeochemical and aeration fluxes computed during the first stage are only applied to DIC from the preceding time step, while TA is calculated after DIC based on the salinity data from the current time step. All subsequent steps are unchanged (Fig. 3b).

Simulations were conducted using both formulations (autochthonous and allochthonous) for the year 2017 (Table 2, SIMC0 and SIMC1).

270 **Table 2. Summary of simulation properties.**

Simulation name	Total Alkalinity	Temperature	Salinity	Air-sea CO <sub>2</sub> fluxes	Biology
<b>SIMC0-Modelled TA (autochthonous formulation)</b>	Modelled	Temperature file	Salinity file	Allowed	Yes
<b>SIMC1-Calculated TA (allochthonous formulation)</b>	Calculated: TA = f(S)	Temperature file	Salinity file	Allowed	Yes
<b>SIMC2-Aeration effect</b>	Calculated: TA = f(S)	Temperature file	Salinity file	Not allowed	Yes
<b>SIMC3-Biology effect</b>	Calculated: TA = f(S)	Temperature file	Salinity file	Not allowed	No
<b>SIMC4-Solubility effect</b>	Calculated: TA = f(S)	Constant: T = 16.4°C	Constant: S = 38.1	Not allowed	No

### 2.3 pCO<sub>2</sub> decomposition

To determine the drivers of temporal variability of pCO<sub>2</sub>, we use two types of pCO<sub>2</sub> decomposition. The first is based on Lovenduski et al. (2007) and evaluates TA, DIC, temperature, and salinity contributions to pCO<sub>2</sub> variations, while the second is based on Turi et al. (2014) and consider the contributions of biology, air-sea CO<sub>2</sub> fluxes and solubility.

#### 275 2.3.1 TA, DIC, T, and S drivers

Following the reasoning presented in Lovenduski et al. (2007), pCO<sub>2</sub> variations can be expressed as the sum of variations generated by changes in TA, DIC, temperature and salinity as follow:

$$\Delta pCO_2 = \Delta pCO_2^{TA} + \Delta pCO_2^{DIC} + \Delta pCO_2^T + \Delta pCO_2^S$$

$$\Delta pCO_2 = \frac{\partial pCO_2}{\partial TA} * (TA - \overline{TA}) + \frac{\partial pCO_2}{\partial DIC} * (DIC - \overline{DIC}) + \frac{\partial pCO_2}{\partial T} * (T - \overline{T}) + \frac{\partial pCO_2}{\partial S} * (S - \overline{S}),$$

280

where  $\Delta pCO_2$  is in  $\mu\text{atm}$ . The overbar in  $\overline{TA}$ ,  $\overline{DIC}$ ,  $\overline{T}$  and  $\overline{S}$  denotes the annual mean. Freshwater inputs can induce changes in TA and DIC. Though, we isolate the changes of TA and DIC due to variations in freshwater inputs using the salinity-

(912)

a mis en forme : Droite

normalised TA (nTA) and DIC (nDIC) which are obtained by dividing the considered variable by in situ salinity and by multiplying the result by mean in situ salinity, and adding another term to regroup them. For simplicity, we only use one term to designate salinity and freshwater inputs. Eq. (912) can thus be rewritten as:

$$\Delta pCO_2 = \Delta pCO_2^{nTA} + \Delta pCO_2^{nDIC} + \Delta pCO_2^T + \Delta pCO_2^{S+FW}$$

$$\Delta pCO_2 = rS * \frac{\partial pCO_2}{\partial TA} * (TA - \overline{TA}) + rS * \frac{\partial pCO_2}{\partial DIC} * (DIC - \overline{DIC}) + \frac{\partial pCO_2}{\partial T} * (T - \overline{T}) + \frac{\partial pCO_2}{\partial S} * (S - \overline{S}) + rS_{TA} * \frac{\partial pCO_2}{\partial TA} * (S - \overline{S}) + rS_{DIC} * \frac{\partial pCO_2}{\partial DIC} * (S - \overline{S}),$$

(1013)

a mis en forme : Droite

where  $rS$  represents the ratio of salinity to mean salinity,  $rS_{TA}$  the ratio of nTA to salinity and  $rS_{DIC}$  the ratio of nDIC to salinity. See Appendix A in Lovenduski et al., (2007) for more details about the computation. Derivatives are obtained using the approach suggested by Sarmiento and Gruber, (2006).

### 2.3.2 Contributing processes

The second decomposition (Turi et al., 2014) aims to estimate the contribution of air-sea  $CO_2$  exchanges, biological processes, and solubility effects to  $pCO_2$  variations:

$$\Delta pCO_2 = \Delta pCO_2^{Aeration} + \Delta pCO_2^{Biology} + \Delta pCO_2^{Solubility}$$

(1014)

a mis en forme : Droite

With the modelling approach used here, we can easily identify the individual processes and evaluate their effect on  $pCO_2$  variations. Several simulations are required to identify and separate the effects of the underlying processes (see Table 2, SIMC2 to SIMC4). SIMC2 aimed to quantify the effect of aeration process on  $pCO_2$  variations. Starting from SIMC1, we disabled the air-sea  $CO_2$  exchanges. SIMC3 aimed to estimate the effects of biology. Using the above reasoning, we deactivated all biological processes, i.e., neither the biology nor aeration was activated in SIMC3. Finally, SIMC4 aimed to evaluate the effect of solubility on  $pCO_2$  variations. This was achieving by keeping both temperature and salinity constant, using their annual means. The first three terms of the Eq. (1014) can be calculated as follow:

$$\Delta pCO_2^{process_i} = pCO_2^{SIMC(i-1)} - pCO_2^{SIMC(i)},$$

(1015)

a mis en forme : Droite

where  $i$  is the simulation number for the process considered ( $2 \leq i \leq 4$ ). The order in which the simulations are run is particularly important. For instance, we quantified the aeration effect (by deactivating aeration) before examining the effect of biological processes (also by deactivating them) because of the impact the biology can have on seawater  $pCO_2$  and on aeration fluxes. Using similar reasoning, the impact of the biology is assessed before the impact of solubility (obtained by

setting temperature and salinity constant) temperature itself has a significant effect on the biology (Lajaunie-Salla et al., 2021).

## 2.4 Statistical indicators

We used three statistical indicators for the comparison between simulation and SOLEMIO data: the percent bias (%BIAS), the cost function (CF) and the root-mean square deviation (RMSD). These indicators were used with two Eco3M\_MIX-CarbOx simulations (SIMC0 and SIMC1) and the reference Eco3M-CarbOx simulation (Lajaunie-Salla et al., 2021).

%BIAS is calculated according to Allen et al. (2007) and allows to quantify the model's tendency to under- or overestimate the observations. In our case, a positive %BIAS means that the model underestimated the in situ observations and vice versa. %BIAS is interpreted according to Marechal (2004). We use the absolute values of %BIAS, to assess the overall agreement between the model results and observations. The agreement is considered: excellent if  $\%BIAS < 10\%$ , very good if  $10\% \leq \%BIAS < 20\%$ , good if  $20\% \leq \%BIAS < 40\%$  and poor otherwise.

The cost function is calculated based on Allen et al. (2007). It is a dimensionless indicator that quantifies the goodness of fit between the model and observations. According to Radaeh and Moll (2006),  $CF < 1$  is considered very good,  $1 \leq CF < 2$  is good,  $2 \leq CF < 3$  is reasonable, while  $CF \geq 3$  is poor.

RMSD quantifies the difference between model results and observations (Allen et al., 2007). The closer RMSD is to 0, the more reliable the model.

All statistical indicators are calculated using surface SOLEMIO data from 2017. The model data is averaged using the mean of the output from the date in question  $\pm$  five days. Using temporal mean and standard deviation of model results allowed us to better account of variability at SOLEMIO station. By comparing the statistical indicators obtained for SIMC0, SIMC1 and Eco3M-CarbOx we also obtained an indication of how changes in the carbonate formulation affected the results.

We used four statistical indicators for the comparison between simulation and SOLEMIO data: the percentage bias (%BIAS), the average error (AE), the average absolute error (AAE) and the root mean square deviation (RMSD, also refer as root mean square error in the literature - RMSE). They were used with two Eco3M\_MIX-CarbOx simulations (SIMC0 and SIMC1) and the reference Eco3M-CarbOx simulation (Lajaunie-Salla et al., 2021). The %BIAS is calculated as follow:

$$\%BIAS = \frac{\sum_{i=1}^N (O_i - M_i)}{\sum_{i=1}^N O_i} * 100$$

where O represents the observations and M the model results (Allen et al., 2007). This indicator allows to quantify the model's tendency to under- or overestimate the observations. The closer the value is to 0, the better the model. Here, a positive %BIAS means that the model underestimated the in situ observations and vice versa. On an indicative basis, the %BIAS can be interpreted according to Marechal (2004): Absolute values of %BIAS allow to assess the overall agreement between the model results and observations and the agreement is considered: excellent if  $\%BIAS < 10\%$ , very good if  $10\% \leq \%BIAS < 20\%$ , good if  $20\% \leq \%BIAS < 40\%$  and poor otherwise.

(16)

a mis en forme : Couleur de police : Automatique

a mis en forme : Couleur de police : Automatique

a mis en forme : Couleur de police : Automatique

a mis en forme : Couleur de police : Automatique

a mis en forme : Couleur de police : Automatique

a mis en forme : Couleur de police : Automatique

a mis en forme : Couleur de police : Automatique

a mis en forme : Couleur de police : Automatique

a mis en forme : Couleur de police : Automatique

a mis en forme : Couleur de police : Automatique

a mis en forme : Couleur de police : Automatique

a mis en forme : Couleur de police : Automatique

a mis en forme : Couleur de police : Automatique



We based our calculation of AE, AAE and RMSD on Stow et al. (2009). Together, these three statistical indicators provide an indication of model prediction accuracy.

$$AE = \frac{\sum_{i=1}^N (O_i - M_i)}{N}$$

(17)

$$AAE = \frac{\sum_{i=1}^N (|O_i - M_i|)}{N}$$

(18)

$$RMSD = \sqrt{\frac{\sum_{i=1}^N (O_i - M_i)^2}{N}}$$

(19)

The three of them aim to measure the size of the discrepancies between model results and observations, the closer the value is to 0, the better the agreement between model results and observations. However, when interpreting AE, it is important to note that value near zero can be misleading because negative and positive discrepancies can cancel each other. That is why it is important to calculate, in addition to AE, AAE and RMSD which allow to overcome this effect (Stow et al., 2009). Such

as %BIAS, a positive value of AE means that the model underestimated the in situ observations and vice versa.

The model data is averaged using the mean of the output from the date in question  $\pm$  five days. Using temporal mean and standard deviation of model results allowed us to better account of variability at SOLEMIO station. By comparing the statistical indicators obtained for SIMC0, SIMC1 and Eco3M-CarbOx we also obtained an indication of how changes in the carbonate formulation affected the results.

### 3 Results

#### 3.1 Carbonate system variables

We performed an initial qualitative evaluation of Eco3M\_MIX-CarbOx, comparing the output of SIMC0 (using the autochthonous TA formulation) and SIMC1 (using allochthonous TA formulation) for TA, DIC,  $pCO_2$  and  $pH_T$  to the corresponding SOLEMIO surface data for 2017 (Figs. 4a-d). The different TA formulations yielded very different model outputs for DIC,  $pCO_2$  and  $pH_T$  (Figs. 4f-h).

a mis en forme : Couleur de police : Automatique

a mis en forme : Couleur de police : Automatique

a mis en forme : Couleur de police : Automatique

a mis en forme : Couleur de police : Automatique

a mis en forme : Couleur de police : Automatique

a mis en forme : Couleur de police : Automatique

a mis en forme : Couleur de police : Automatique

a mis en forme : Couleur de police : Automatique

a mis en forme : Couleur de police : Automatique

a mis en forme : Couleur de police : Automatique

a mis en forme : Couleur de police : Automatique

a mis en forme : Couleur de police : Automatique

a mis en forme : Couleur de police : Automatique

a mis en forme : Couleur de police : Automatique

a mis en forme : Couleur de police : Automatique

a mis en forme : Couleur de police : Automatique

a mis en forme : Couleur de police : Automatique

a mis en forme : Couleur de police : Automatique

a mis en forme : Couleur de police : Automatique

a mis en forme : Couleur de police : Automatique

a mis en forme : Couleur de police : Automatique

a mis en forme : Couleur de police : Automatique

a mis en forme : Couleur de police : Automatique

a mis en forme : Couleur de police : Automatique

a mis en forme : Couleur de police : Automatique

a mis en forme : Couleur de police : Automatique

a mis en forme : Couleur de police : Automatique

a mis en forme : Couleur de police : Automatique

a mis en forme : Couleur de police : Automatique

a mis en forme : Couleur de police : Automatique

a mis en forme : Couleur de police : Automatique

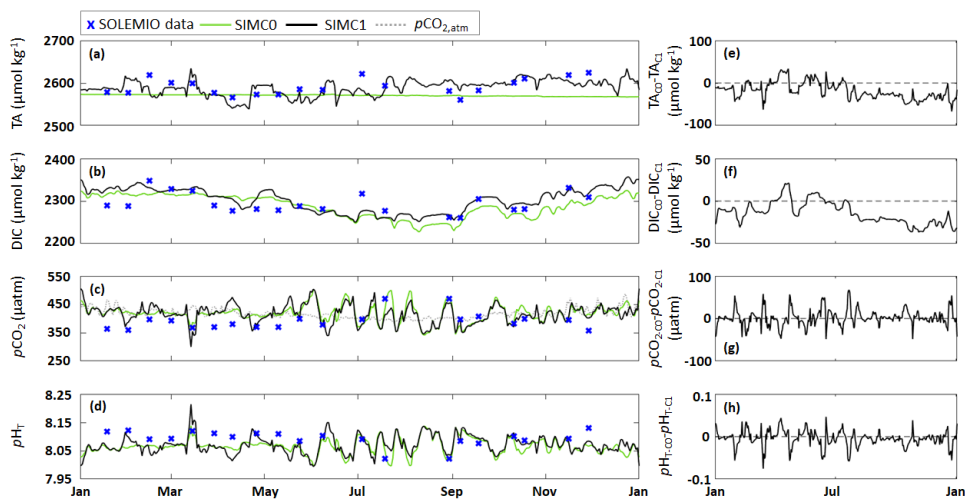


**Figure 4.** (a-d) Comparison of model outputs from the SIMC0 (autochthonous formulation) and SIMC1 (allochthonous formulation), model runs showing daily averages of (a) TA, (b) DIC, (c) seawater  $p\text{CO}_2$  and CAV atmospheric  $p\text{CO}_2$  and (d)  $\text{pH}_r$ . (e-h) Differences between SIMC0 and SIMC1 outputs for each variable ( $\text{VARC0} - \text{VARC1}$ ).

- 370 TA observations varied between  $2560.8$  and  $2623.9 \mu\text{mol kg}^{-1}$ , with no apparent seasonal pattern (Fig. 4a). This variability is successfully represented by SIMC1, but not SIMC0 (SIMC1 range:  $2540$  to  $2635 \mu\text{mol kg}^{-1}$ ). SIMC0 produces TA values that show a gradual and near-linear decrease from  $2578 \mu\text{mol kg}^{-1}$  in early January to  $2572 \mu\text{mol kg}^{-1}$  at the end of the year. The differences between SIMC0 and SIMC1 are most pronounced between August and December where SIMC1 delivers systematically higher TA values compared to SIMC0 (Fig. 4e).
- 375 With regard to DIC, both SIMC0 and SIMC1 are capable of reproducing the seasonal variability present in the in situ data. From November to April, DIC has higher values (around  $2320 \mu\text{mol kg}^{-1}$  in both simulations), with lower values during the rest of the year (both have a minimum August, SIMC0:  $2234 \mu\text{mol kg}^{-1}$  and SIMC1:  $2254 \mu\text{mol kg}^{-1}$ ; Fig. 4b). At the beginning of the year, SIMC1 seems to be closer to the observations than SIMC0 which shows fewer variations (e.g., SIMC1 appears to be better at reproducing the decrease visible at the end of April). Differences between SIMC0 and SIMC1 for DIC
- 380 are similar to those observed for TA (Fig. 4e,f) although in absolute terms, they are only about half of what we observed for TA. Nevertheless, these results show that the choice of the TA formulation strongly affects the DIC model results (Fig. 4f). The in situ  $p\text{CO}_2$  data exhibits strong variations throughout the year, especially from May to November which are well represented in both simulations (Fig. 4c). Between January and April, both simulations overestimate the in situ  $p\text{CO}_2$  values: while the simulations both predict  $p\text{CO}_2$  values close to the CAV atmospheric  $p\text{CO}_2$  of about  $415 \mu\text{atm}$ ,  $p\text{CO}_2$  observed at
- 385 SOLEMIO is lower indicating under-saturation. For both simulations yield a strong decrease of  $p\text{CO}_2$  is modelled on

March 15<sup>th</sup>, in response to a Rhône River intrusion in the BoM. This event is particularly marked in the SIMC1 model results which show a decrease from 450 to 300  $\mu\text{atm}$  (compared to a decrease from 415 to 358  $\mu\text{atm}$  with SIMC0). While this decrease is also visible in the in situ data it is more moderate (392 to 367  $\mu\text{atm}$ ).

Regarding  $p\text{H}_T$ , both simulations produced similar dynamics as for  $p\text{CO}_2$  (Figs. 4d vs 4c). Both simulations deliver good representations of the observed  $p\text{H}_T$  variations between May and November while from January to April both simulations underestimate the in situ (in situ: 8.12 vs simulations: 8.07). The Rhône River intrusion is also visible in the  $p\text{H}_T$  data which exhibits a sudden increase. While both simulations show this increase, it is more pronounced in the SIMC1 results (increase from 8.04 to 8.21) compared to SIMC0 (8.07 to 8.14), but in both cases larger than in the observations (8.09 to 8.12).

The differences between both simulations for  $p\text{CO}_2$  and  $p\text{H}_T$  do not exhibit any noticeable trend (Fig. 4g,h). However, looking at the annual average, SIMC1 produces lower (higher)  $p\text{CO}_2$  ( $p\text{H}_T$ ) values compared to SIMC0 with a mean difference of 2.3  $\mu\text{atm}$  ( $-5 \times 10^{-3}$ ). Moreover, for both variables, the differences between SIMC0 and SIMC1 are more pronounced at the beginning of the year.

Regarding the coast function, simulations yielded  $\text{CF} < 2$  for all variables which is considered very good ( $\text{CF} < 1$ ) or good ( $1 \leq \text{CF} < 2$ ) (Table 3). The %BIAS parameter yielded “excellent” results for all variables (using the interpretation form Marechal, 2004, i.e., %BIAS  $< 10\%$ ). The highest values for %BIAS (in absolute terms) were obtained for  $p\text{CO}_2$  with  $-6\%$  while the remaining variables had values  $< 1\%$ . Similarly,  $p\text{CO}_2$  had the highest RMSD which suggests that this parameter is not as well represented in the model as the other variables.

Furthermore, SIMC1 produced the best TA representation yielding the lowest values for CF, %BIAS and RMSD (Table 3). Moreover, SIMC1 produced an annual mean TA that was closest to the observations. While the SIMC0 and Eco3m-CarbOx results are fairly similar, SIMC0 produced a slightly better representation of TA compared to Eco3m-CarbOx. Similar conclusions can be drawn for  $p\text{H}_T$  where SIMC1 also outperformed SIMC0 based on CF and %BIAS (Table 3). For studying DIC and  $p\text{CO}_2$ , the situation is less clear as the simulations performed differently for different indicators, making it difficult to pick a clear winner. Still SIMC1 shows the best CF and RMSD values for DIC, and the best CF and %BIAS for  $p\text{CO}_2$ . In conclusion, SIMC1 shows the best overall indicator values for the examined variables (more specifically, it outperformed the other simulations in 9 of 12 indicator comparisons).

For statistical indicators, %BIAS values are systematically lower than 10 %, with the highest values obtained for  $p\text{CO}_2$  with  $-6\%$  while the remaining variables had values  $< 1\%$ . Similarly,  $p\text{CO}_2$  had the highest RMSD, AAE and AE which suggests that this parameter is not as well represented in the model as the other variables. Furthermore, SIMC1 produced the best TA representation resulting in the lowest values for %BIAS, AE, AAE and RMSD (Table 3). Moreover, SIMC1 produced an annual mean TA that was closest to the observations. While the SIMC0 and Eco3m-CarbOx results are fairly similar, SIMC0 produced a slightly better representation of TA compared to Eco3m-CarbOx (%BIAS, AE, AAE and RMSD slightly lower). For  $p\text{H}_T$ , SIMC1 outperformed SIMC0 based on %BIAS (Table 3), however, AE, AAE and RMSD values are similar for the three simulations. We then performed the calculation of statistical indicators on  $\text{H}_4^+$  concentration as, according to some authors (Kwiatkowski & Orr, 2018), comparing  $\text{H}_4^+$  concentrations is a better practice than comparing  $p\text{H}$ .

a mis en forme : Police :Italique

a mis en forme : Indice

a mis en forme : Indice

a mis en forme : Exposant

a mis en forme : Exposant

420 Results are available in Appendix C. Based on Table C1, SIMC1 also outperformed SIMC0 based on AE and AAE. For  
 425 studying DIC and  $p\text{CO}_2$ , the situation is less clear as the simulations performed differently for different indicators, making it  
 difficult to pick a clear winner. Still SIMC1 shows the best AAE and RMSD values for DIC, and the best %BIAS, AE, and  
 AAE for  $p\text{CO}_2$ . In conclusion, SIMC1 shows the best overall indicator values for the examined variables (more specifically,  
 it outperformed the other simulations in 13 of 20 indicator comparisons when including  $\text{H}_2\text{CO}_3^*$  concentrations comparison).

**Table 3. Comparing the different model results to surface observations at SOLEMIO station for TA, DIC, seawater  $p\text{CO}_2$ , and  $\text{pH}_T$ .** N represents the number of observations. Mean, SD, AE, AAE and RMSD are in the same unit than the considered variable, i.e.:  $\mu\text{mol kg}^{-1}$  for TA and DIC and  $\mu\text{atm}$  for  $p\text{CO}_2$ . % BIAS is without unit.

		TA	DIC	$p\text{CO}_2$	$\text{pH}_T$
<b>N</b>	Observations	20	20	20	20
<b>Mean <math>\pm</math> SD</b>	Observations	2591.2 $\pm$ 19.4	2294.9 $\pm$ 24.0	391.0 $\pm$ 31.0	8.09 $\pm$ 0.030
	SIMC0	2576.1 $\pm$ 1.5	2293.6 $\pm$ 25.1	413.5 $\pm$ 16.5	8.07 $\pm$ 0.015
<b>Mean <math>\pm</math> SD</b>	SIMC1	2588.6 $\pm$ 16.4	2301.1 $\pm$ 24.5	409.1 $\pm$ 21.4	8.07 $\pm$ 0.020
	CarbOx <del>x</del>	2574.5 $\pm$ 3.6	2292.5 $\pm$ 26.0	413.9 $\pm$ 15.9	8.07 $\pm$ 0.010
<b>CF</b>	<del>SIMC0</del>	<del>0.96</del>	<del>0.85</del>	<del>1.16</del>	<del>1.20</del>
	<del>SIMC1</del>	<del>0.84</del>	<del>0.71</del>	<del>1.12</del>	<del>1.11</del>
	<del>CarbOx</del>	<del>1.03</del>	<del>0.88</del>	<del>1.14</del>	<del>1.18</del>
<b>%BIAS</b>	SIMC0	0.58	0.05	-5.75	0.29
	SIMC1	0.09	-0.27	-4.61	0.21
	CarbOx	0.64	0.1	-5.86	0.29
<b>AE</b>	<del>SIMC0</del>	<del>15.12</del>	<del>1.25</del>	<del>-22.5</del>	<del>0.02</del>
	<del>SIMC1</del>	<del>2.57</del>	<del>-6.2</del>	<del>-18.02</del>	<del>0.02</del>
	<del>CarbOx</del>	<del>16.7</del>	<del>2.4</del>	<del>-22.9</del>	<del>0.02</del>
<b>AAE</b>	<del>SIMC0</del>	<del>18.7</del>	<del>20.4</del>	<del>35.9</del>	<del>0.03</del>
	<del>SIMC1</del>	<del>16.3</del>	<del>17.2</del>	<del>34.7</del>	<del>0.03</del>
	<del>CarbOx</del>	<del>20.1</del>	<del>21.2</del>	<del>35.3</del>	<del>0.03</del>
<b>RMSD</b>	SIMC0	24.90	24.26	38.75	0.04
	SIMC1	20.03	21.83	40.27	0.04
	CarbOx	26.56	24.90	38.29	0.04

a mis en forme : Police :Italique

a mis en forme : Indice

a mis en forme : Police :Italique

a mis en forme : Indice

a mis en forme : Exposant

a mis en forme : Exposant

a mis en forme : Police :Italique

a mis en forme : Indice

### 3.2 Air-sea CO<sub>2</sub> fluxes

430 Throughout 2017 temperature varied from 13.3 to 25.9 °C (Fig. 5a) with the highest variability visible during the summer upwelling period (SUP) (Fig. 5e). Apart from four low salinity events in March, May, June, and September (all corresponding to the Rhône River intrusions) the salinity remained close to its mean value of 38.1 (Fig. 5a).

Wind speed was highly variable with several strong gusts, especially during winter when wind speeds often exceeded 10 m s<sup>-1</sup> (Fig. 5b). Wind speed tends to be lower during summer and SUP, although these periods also show numerous strong wind events (> 10 m s<sup>-1</sup>) (Fig. 5f).

435 The sea-air pCO<sub>2</sub> difference exhibits the same seasonality as temperature, with high positive values during summer while oscillating about zero during the rest of the year. In general, the sea-air pCO<sub>2</sub> difference combines the patterns from temperature, salinity and wind speed which are the main underlying forcings. The local minimum in March, corresponds to an extremely low salinity event (Fig. 5c). However, during the SUP the sea-air pCO<sub>2</sub> difference is mostly driven by temperature (Fig. 5g) as seen by the high variability between May and October which coincide with the largest temperature variations.

440 In contrast, air-sea CO<sub>2</sub> fluxes do not show any seasonality, with values oscillating about zero throughout the year (Fig. 5d) yielding an integrated total of -0.21 mmol m<sup>-2</sup> per year. Maximum positive values are obtained from November to March when wind speeds are highest. Extreme negative value (-13 mmol m<sup>-2</sup> per day) can be seen in July coinciding with high wind speed, negative sea-air pCO<sub>2</sub> difference and a significant drop in temperature.

445 speed, negative sea-air pCO<sub>2</sub> difference and a significant drop in temperature.

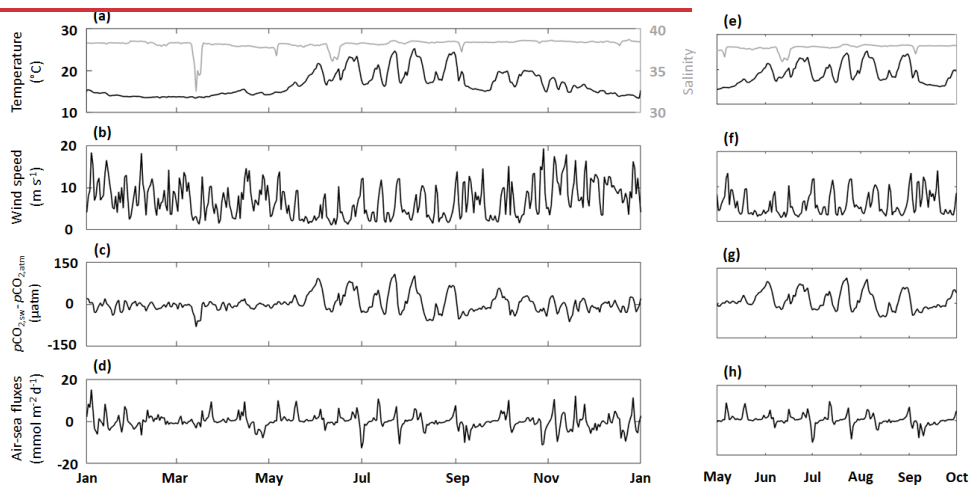


Figure 5. Time series of (a, e) in situ daily average sea surface temperature (black line) and salinity (grey line) (b, f) SIMCI daily average wind speed (c, g) the difference between SIMCI daily average seawater pCO<sub>2</sub> and in situ daily average atmospheric pCO<sub>2</sub>

(d, h) SIMC1 daily average air-sea CO<sub>2</sub> fluxes (aeration process). (a-d) show the entire year of 2017 while (e-h) focus on the summer upwelling period (SUP), from 1 May to 1 October.

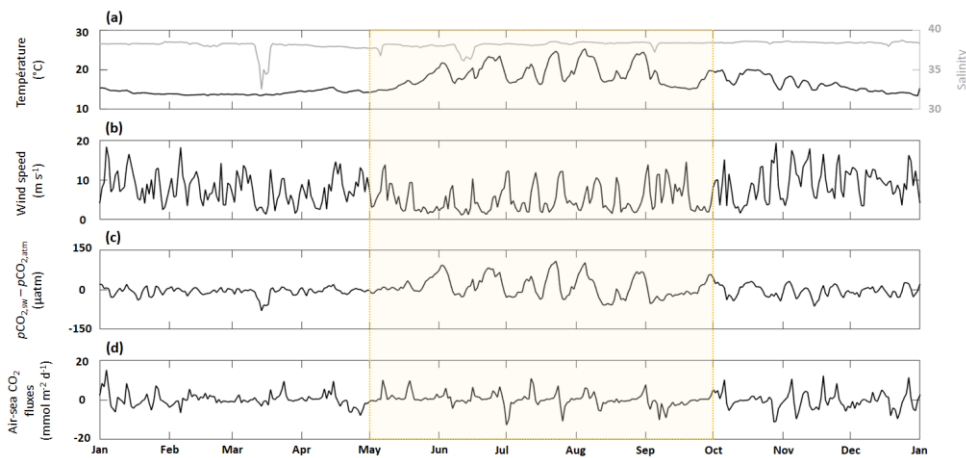


Figure 5. Time series of (a) in situ daily average sea surface temperature (black line) and salinity (grey line) (b) SIMC1 daily average wind speed (c) the difference between SIMC1 daily average seawater pCO<sub>2</sub> and in situ daily average atmospheric pCO<sub>2</sub> (d) SIMC1 daily average air-sea CO<sub>2</sub> fluxes (aeration process). The summer upwelling period (from 1 May to 1 October) is highlighted in yellow.

### 3.3 Main drivers of pCO<sub>2</sub> dynamics

#### 3.3.1 Annual scale

Following the approach from Lovenduski et al. (2007), we used temperature (Fig. 6a), as well as salinity (S), freshwater inputs (Fw), nTA and nDIC (Fig. 6b) contributions to identify the underlying dynamics in the observed pCO<sub>2</sub> variations (Fig. 6c). Seasonal variations in temperature (Fig. 6a) produce seasonal anomalies in pCO<sub>2</sub> with negative anomalies dominating from November to May and mostly positive anomalies throughout the remainder of the year (Fig. 6d). Anomalies generated by S+Fw do not exhibit any seasonality but remain close to zero throughout the year, unless there is an LSE, during which the anomalies turn negative (-101 µatm, -30 µatm, -40 µatm and -20 µatm for the four LSE). Anomalies generated by nDIC show the opposite seasonal trend compared to the anomalies generated by temperature, i.e., from November to May the nDIC-generated anomalies are positive and negative during the rest of the year. The four LSE are also clearly visible in the nDIC-generated anomalies which exhibit sharp increases (increase of 506 µatm, 253 µatm, 243 µatm and 152 µatm respectively). Also, nTA does not produce any seasonality in the anomalies but exhibits sharp decrease during the four LSE (decrease of 548 µatm, 242 µatm, 239 µatm and 90 µatm respectively).

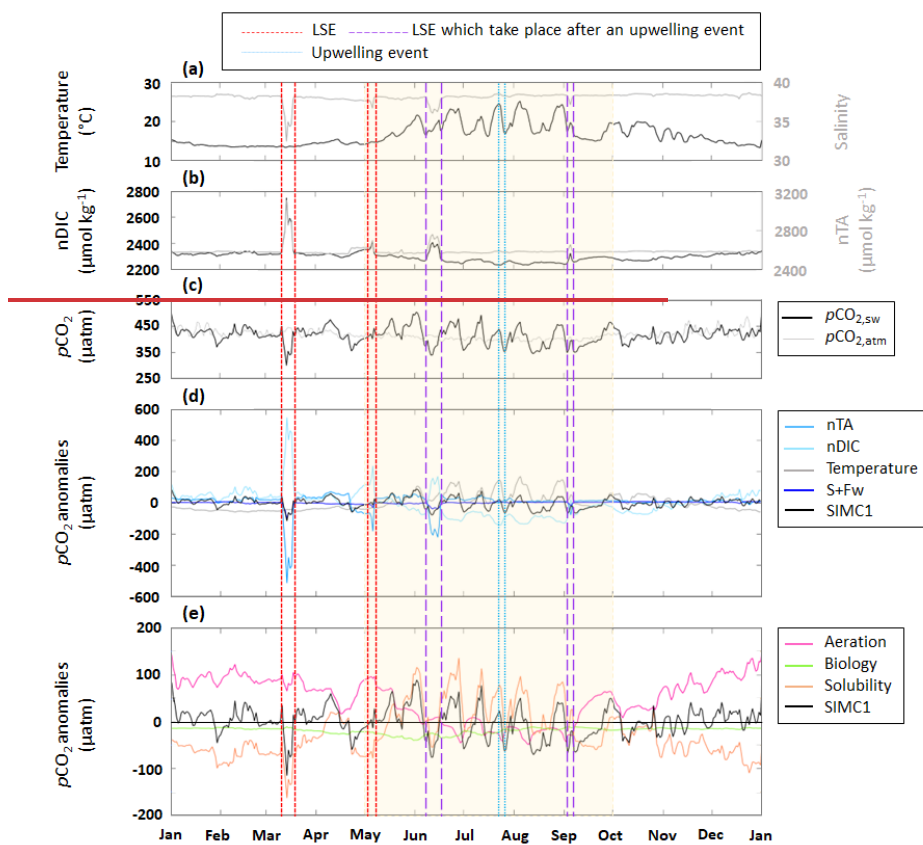
a mis en forme : Police :Italique

a mis en forme : Indice

a mis en forme : Police :Italique

a mis en forme : Indice

a mis en forme : Indice



470 **Figure 6.** Time-series for 2017 of daily average (a) in-situ temperature and salinity (b) modelled nDIC and nTA (c) modelled seawater and in-situ atmospheric  $p\text{CO}_2$  (d)  $p\text{CO}_2$  anomalies generated by DIC, TA, Fw-S and temperature based on the approach in Lovenduski et al. (2007) (Note: the dark blue line is sometimes obscured by the black line, especially in March) (e, j)  $p\text{CO}_2$  anomalies generated by aeration, solubility, and biological processes based on the approach in Turi et al. (2014). LSE and an upwelling event have been highlighted. The summer upwelling period (SUP) is indicated by yellow shading.

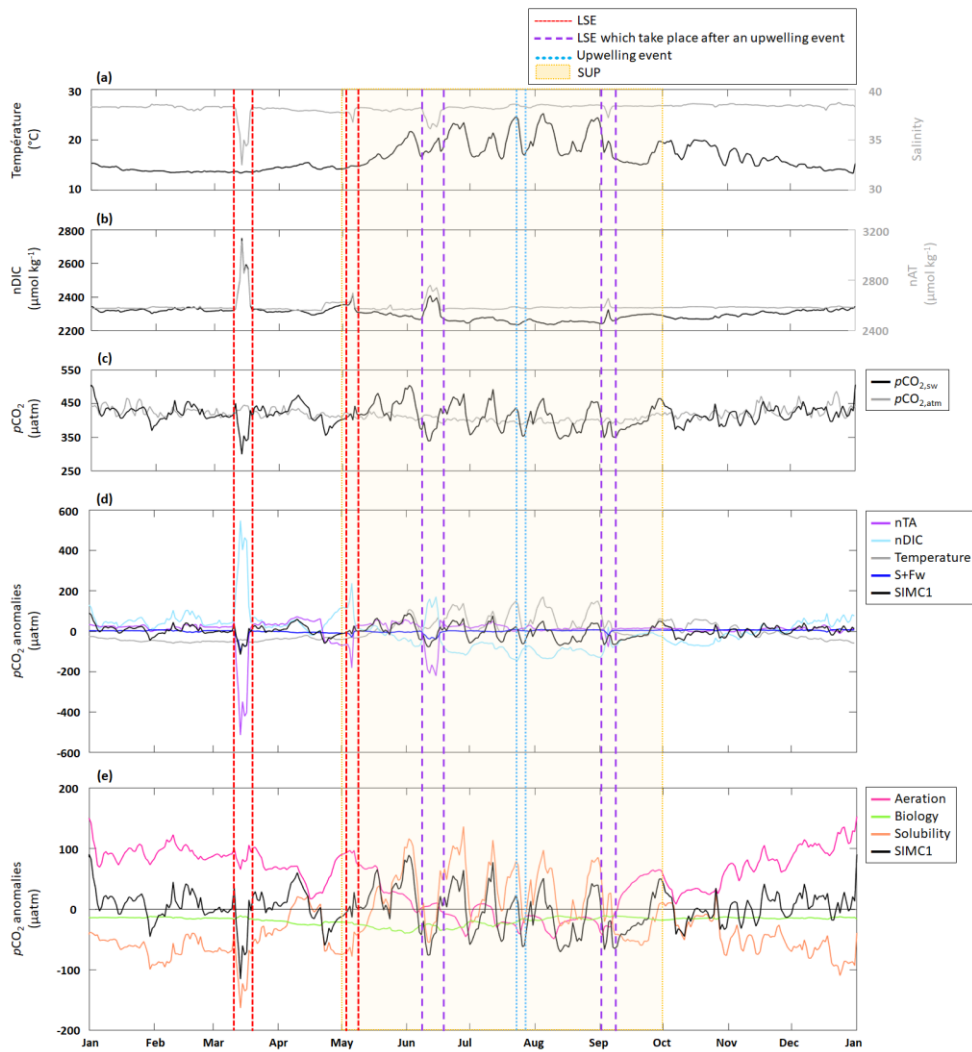


Figure 6. Time series for 2017 of daily average (a) in situ temperature and salinity (b) modelled nDIC and nTA (c) modelled seawater and in situ atmospheric  $p\text{CO}_2$  (d)  $p\text{CO}_2$  anomalies generated by DIC, TA, Fw+S and temperature based on the approach in Lovenduski et al. (2007) (Note: the dark blue line is sometimes obscured by the black line, especially in March. An enlargement

a mis en forme : Police :Italique

a mis en forme : Indice

a mis en forme : Police :Italique

a mis en forme : Indice



480 of the panel d is available in Appendix D) (e, i)  $p\text{CO}_2$  anomalies generated by aeration, solubility, and biological processes based on  
the approach in Turi et al. (2014). LSE and an upwelling event have been highlighted. The summer upwelling period (SUP) is  
indicated by yellow shading.

Following the approach by Turi et al. (2014), we examined the effects of aeration, biological processes, and solubility on  
 $p\text{CO}_2$  variability (Fig. 6e). Aeration produced anomalies very similar to those observed for nDIC (Fig. 6d): positive from  
November to May and negative during the rest of the year. Since  $\text{CO}_2$  solubility is controlled by temperature and salinity,  
485 solubility-generated anomalies essentially follow the trends and seasonality seen in temperature and S+Fw-generated  
anomalies (Fig. 6d): negative from November to May and mostly positive during the rest of the year (mean of  $+9.2 \mu\text{atm}$ ).

The four LSE are also visible in the solubility-generated anomalies generating strong decreases (Fig. 6e). However, only two  
LSE are easily identifiable (15 March with a drop from  $-41 \mu\text{atm}$  to  $-163 \mu\text{atm}$  and 6 May with a drop from  $8 \mu\text{atm}$  to  $-75 \mu\text{atm}$ ) while the other two appear to be obscured by temperature-related counter-movements. Since aeration- and solubility-  
490 generated anomalies show opposite seasonality, they partly cancel each other out. While aeration seems to dominate from  
November to May, (apart from LSE), solubility appears to dominate from May to November and during LSE. Biological  
processes are never the dominant driver of  $p\text{CO}_2$  variations as they are systematically smaller (by a factor of 2 to 3) than  
aeration and solubility-generated anomalies (Fig. 6e). Biology-induced anomalies are always negative, providing evidence  
that biological processes always decrease  $p\text{CO}_2$ .

### 495 3.3.2 During the summer upwelling period (SUP)

The SUP is characterized by significant temperature variations (Fig. 6a) due to periodic upwelling events. During the 2017  
SUP, there were three LSE which will be excluded here as we discuss them in the following section. nTA is nearly constant  
during the SUP while nDIC shows marked variations (Fig. 6b) that are directly linked to variations in DIC (see Section 3.1).  
 $p\text{CO}_2$  is also highly variable during the SUP (Fig. 6c). Using the approach from Lovenduski et al. (2007) (Fig. 6d), the SUP  
500 is characterized by a strong contribution of temperature which shows strong positive anomalies (maximum of  $170 \mu\text{atm}$   
reached on 5 August), and nDIC which shows strong negative anomalies (minimum of  $-142 \mu\text{atm}$  reached on 24 July). S+Fw  
and nTA do not represent significant drivers with anomalies remaining close to zero. Using the approach in Turi et al. (2014)  
(Fig. 6e), we can see that solubility is a major driver producing large amplitude variations in the  $p\text{CO}_2$  anomalies connected  
to similar variations in temperature (a drop in temperature causes the anomaly to change from positive to negative and vice  
505 versa) (Fig. 6a). Aeration, which mostly generates negative anomalies, counteracts solubility. During the SUP, we also  
observed an increase of biological processes contribution since associated anomalies further decrease at the beginning of the  
period (from  $-22 \mu\text{atm}$  on 1 May to  $-40 \mu\text{atm}$  on 31 May).

Focusing on the upwelling event that took place between 23-27 July, we observe a sharp decrease in temperature (from  $24.6$   
 $^\circ\text{C}$  to  $16.9 \text{ }^\circ\text{C}$ ; Fig. 6a), no variation in nTA, and a slight increase in nDIC (from  $2242 \mu\text{mol kg}^{-1}$  to  $2269 \mu\text{mol kg}^{-1}$ ; Fig. 6b).

510 The event is also associated with a strong  $p\text{CO}_2$  decrease (from  $438 \mu\text{atm}$  to  $353 \mu\text{atm}$ ; Fig. 6c). Using the approach in  
Lovenduski et al., (2007) we observed a decrease of the temperature-generated anomaly (from  $148 \mu\text{atm}$  at the beginning of

a mis en forme : Police :Italique

a mis en forme : Indice

the event to 5  $\mu\text{atm}$  at the peak of the event). At the same time, the nDIC-generated anomaly become less negative (from -142  $\mu\text{atm}$  at the beginning of the event to -79  $\mu\text{atm}$  at the peak of the event). Neither nTA nor S+Fw seem to have any significant impact on  $p\text{CO}_2$  anomalies. Using the approach in Turi et al. (2014) (Fig. 6e), the upwelling event is characterized by decrease of solubility-generated anomalies (from 79  $\mu\text{atm}$  at the beginning of the event to -24  $\mu\text{atm}$  at the end of the event). Anomalies generated by aeration and biological processes tend to respectively become positive and less negative at the end of the event (aeration: -45  $\mu\text{atm}$  to 3  $\mu\text{atm}$  ; biological processes: -30  $\mu\text{atm}$  to -20  $\mu\text{atm}$ ).

### 3.3.3 During a low salinity event (LSE)

There were four LSE during 2017: on 15 March, 6 May, 15 June, and 5 September. All four LSE show similar patterns, namely strong decrease in salinity (Fig. 6a) which in turn leads to an increase in both nTA and nDIC (Fig. 6, Table 4). Apart from the 5 September LSE which shows an increase in  $p\text{CO}_2$ , the remaining LSE coincide with significant  $p\text{CO}_2$  decreases (Fig. 6c, Table 4).

**Table 4. Change in S, nTA, nDIC and  $p\text{CO}_2$  from before to during a LSE.**

	S	nTA ( $\mu\text{mol kg}^{-1}$ )	nDIC ( $\mu\text{mol kg}^{-1}$ )	$p\text{CO}_2$ ( $\mu\text{atm}$ )
<b>15 March</b>	38.3 to 32.5	2570 to 3110	2320 to 2750	450 to 300
<b>6 May</b>	37.8 to 36.7	2560 to 2700	2308 to 2420	420 to 401
<b>15 June</b>	38.1 to 36.0	2580 to 2760	2273 to 2409	504 to 340
<b>5 September</b>	38.3 to 37.1	2583 to 2658	2241 to 2327	348 to 396

When using Lovenduski et al., (2007) approach, LSE that do not take place immediately after an upwelling event (i.e., 15 March and 6 May) exhibit similar combinations of driver contributions, e.g., nTA and S+Fw create strong negative anomalies in both LSE (with combined (nTA+S+Fw) contributions of: -614  $\mu\text{atm}$  on 15 March and -211  $\mu\text{atm}$  on 6 May), which are partially cancelled out by nDIC opposite contribution (547  $\mu\text{atm}$  on 15 March and 235  $\mu\text{atm}$  on 6 May). While temperature-generated anomalies showed no change during either event, it is still negative and by adding its effect to those obtained for nTA and S+Fw, we obtain a combined effect of -656  $\mu\text{atm}$  on 15 March and -241  $\mu\text{atm}$  on 6 May.

LSE that take place immediately after a summer upwelling event (i.e., 15 June and 5 September), show similar variations of salinity, nTA, nDIC and  $p\text{CO}_2$  but also show an increase of temperature (from 16.5  $^{\circ}\text{C}$  to 20.5  $^{\circ}\text{C}$  on 15 June and 17.5  $^{\circ}\text{C}$  to 19.8  $^{\circ}\text{C}$  on 5 September; Fig. 6a). Also, the factors driving the anomalies are similar to those for the non-upwelling related LSE discussed in the previous paragraph. The combined nTA and S+Fw anomalies (-260  $\mu\text{atm}$  on 15 June and -108  $\mu\text{atm}$  on 5 September) are partially compensated by nDIC contribution (171  $\mu\text{atm}$  and 22  $\mu\text{atm}$  respectively). Unlike for the previous events, we do see a significant temperature effect for the upwelling-related LSE: temperature-generated anomalies are positive (45  $\mu\text{atm}$  on 15 June and 53  $\mu\text{atm}$  on 5 September) and support nDIC contribution.

When following Turi et al. (2014) (Fig. 6e), all LSE, with the exception of the 5 September LSE, are characterized by strong negative solubility-generated anomalies (-163  $\mu\text{atm}$  on 15 March, -78  $\mu\text{atm}$  on 6 May and -55  $\mu\text{atm}$  on 15 June) partially compensated by positive aeration-generated anomalies (65  $\mu\text{atm}$ , 97  $\mu\text{atm}$  and 8  $\mu\text{atm}$  respectively). The odd one out which take place on 5 September shows positive solubility-generated anomaly (27  $\mu\text{atm}$ ) and negative aeration-generated anomaly (-30  $\mu\text{atm}$ ). In all the four LSE, biological processes did not have any significant impact on  $p\text{CO}_2$  variations (anomalies generated by biological processes are 2 to 3 times lower than those generated by aeration or solubility).

## 4 Discussion

### 4.1 Impact of Rhône River inputs on TA variations

Due to its location near the Rhône River mouth, the BoM is particularly affected by freshwater inputs. In 2017, there were four LSE in the BoM. Apart from being low in salinity, the Rhone River water entering the BoM also contains organic matter, nutrients, DIC and alkalinity, with a mean TA of 2885  $\mu\text{mol kg}^{-1}$  (Schneider et al., 2007). This input adds up to the effect of biological processes. We have seen that TA measurements in the BoM exhibit significant variability throughout the year (Fig. 4a), although no obvious seasonality. By considering autochthonous (i.e., dependant on biological processes only) and allochthonous (i.e., dependant on rivers inputs only) formulations of TA, we were able to isolate the effects of the biology and riverine inputs and quantify their relative importance for the TA variations seen in the BoM.

With the autochthonous formulation, TA remained fairly constant throughout the year, which is similar to the results obtained by Lajaunie-Salla et al. (2021). In contrast, the allochthonous formulation ~~produced~~ ~~yielded~~ a much high variability in TA that was close to in situ observations. Several authors suggested that biological processes could have a large effect on TA dynamics in coastal areas (Krumins et al., 2013; Gustafsson et al., 2014). These findings are not confirmed by our model results where changes in TA due to biology did not exceed 5  $\mu\text{mol kg}^{-1}$  (Fig. 4a), which is insignificant compared to the changes attributed to other drivers, including riverine inputs. This suggests that TA variations in the BoM are mostly driven by allochthonous factors. The importance of allochthonous contributions to TA variations have already been highlighted by several authors at the Mediterranean Sea scale (Copin-Montegut, 1993; Schneider et al., 2007; Hassoun et al., 2015). Other important drivers in the Mediterranean include TA exchanges with the Atlantic Ocean and Black Sea, as well as TA inputs from sediments and rain. For the particular location of our study area, we only considered river contributions. Having neglected other allochthonous drivers seems to be justified by the results which ~~showed~~ ~~yielded~~ a close match to observations and a generally better representation of the other carbonate system variables since DIC,  $p\text{CO}_2$  and  $\text{pH}_T$  are all closely related to TA (Fig. 4 and Table 3). Several studies of TA variations in the Mediterranean Sea have been conducted at the sub-basins scale yielding different TA-S correlation for different study areas (Cossarini et al., 2015; Hassoun et al., 2015). For instance, the correlation proposed for the north-western Mediterranean Sea, suggests that local TA dynamics are mainly controlled by evaporation. We did not include this in our study as the BoM is strongly impacted by the Rhône River. By focussing on a smaller area, we ~~could~~ ~~not~~ provide a TA formulation that represents this particular part of the Mediterranean very well.

570 While our results seem to provide a realistic representation of TA dynamics in the BoM, we could have included other  
factors such as sediments, which have been shown to be important for TA dynamics, particularly in coastal areas (Brenner et  
al., 2016; Gustafsson et al., 2014). We plan to add TA supplies by sediments in our future work.

## 4.2 Impact of hydrodynamic processes on $p\text{CO}_2$ variations

### 4.2.1 Low salinity events (LSE)

575 The four LSE observed in 2017 had several common characteristics: a salinity decrease (Fig. 6a) and apparent nTA and  
nDIC increases (Fig. 6b). Three of the four LSE resulted in a  $p\text{CO}_2$  decrease (15 March, 6 May, and 15 June, Fig. 6c). Rhône  
River intrusion events are often associated with a  $p\text{CO}_2$  decrease since the introduced nutrients stimulate phytoplanktonic  
growth (Frayse et al., 2014; Lajaunie-Salla et al., 2021). However, in our case, the decrease of  $p\text{CO}_2$  observed on 15 March,  
6 May and 15 June was entirely caused by nTA and solubility effects (Figs. 6d,e). Generally, a TA increase is associated  
580 with a  $p\text{CO}_2$  decrease that is proportional to the buffering state of the considered water mass (for high TA:DIC ratios,  
changes in  $p\text{CO}_2$  are lower since the water mass is well buffered; Middelburg et al., 2020), which explains the negative  $p\text{CO}_2$   
anomalies associated with these three LSE. Solubility depends on both salinity and temperature. Depending on the size and  
the duration of the Rhône River intrusion, salinity effect to solubility can vary. When salinity is decreasing, the solubility of  
 $\text{CO}_2$  in seawater also decreases, which results in a decrease in  $p\text{CO}_2$  (Middelburg, 2019). The effects of temperature to  
solubility vary throughout the year. For instance, during the 15 March and 6 May LSE, temperatures were low and fairly  
585 constant (Fig. 6a) and therefore only contributed a small amount to the negative anomaly (Fig. 6d). In contrast, the 15 June,  
temperature cause a positive  $p\text{CO}_2$  anomaly (Fig. 6d). This difference can be explained by the fact that the 15 June LSE took  
place right after an upwelling event, probably facilitated by the Marseille eddy presence near the BoM, which tend to be  
observed just after Mistral events (Frayse et al., 2014). While the temperature dropped as a result of the upwelling, once the  
590 event was over the temperature increased again which caused the observed positive  $p\text{CO}_2$  anomaly. Despite this positive  
temperature-related anomaly, the overall anomaly remained negative due to the strong effects of salinity and nTA during the  
LSE (Fig. 6c).

The 5 September LSE was associated with a  $p\text{CO}_2$  increase (Fig. 6c), caused by nDIC and solubility effects (Figs. 6d,e): as  
salinity and nTA contributions remain weak, they are completely counterbalanced by nDIC and temperature contribution,  
595 resulting in an increase of  $p\text{CO}_2$ . During September 5th LSE, observed salinity and temperature showed opposite patterns:  
the decrease of salinity is associated to an increase of temperature, and the increase of salinity after the peak of the LSE, is  
associated to a temperature decrease (Fig. 6a). Unlike for the 15 June LSE, the temperature increase seen during the 5  
September event was not caused by the end of the upwelling event preceding as the temperature was decreasing right after  
the LSE peak (Fig. 6a). We assume that this temperature increase was instead caused by the intruding Rhône River water,  
600 which brought about the observed  $p\text{CO}_2$  increase ( $p\text{CO}_2$  increases exponentially with temperature; Middelburg, 2019).

In all four LSE, biological processes did not have any significant impact on  $p\text{CO}_2$  variations (Fig. 6e). While we only considered TA inputs, Rhône River intrusion can also bring nutrients (Frayse et al., 2014). In all four LSE, biological processes did not have any significant impact on  $p\text{CO}_2$  variations (Fig. 6e). To interpret this result, it is important to consider the assumptions used by Eco3M MIX-CarbOx (section 2.2). Rhône River intrusion can significantly modify the biogeochemistry of the bay as they are typically associated with temperature and salinity changes and TA, DIC and nutrients inputs (Gatti et al., 2006; Frayse et al., 2014; Lajaunie-Salla et al., 2021). Due to its 0D configuration, Eco3M MIX-CarbOx only represents temperature and salinity changes and TA inputs (only if the allochthonous formulation is used for the latter, Fig. 2). Lajaunie-Salla et al. (2021) showed that these nutrient inputs led to an increase in chlorophyll concentration. This phytoplankton growth leads to further decrease in  $p\text{CO}_2$ , which means that by neglecting nutrient inputs we possibly underestimated the importance of biological processes, and especially of autotrophic processes during Rhône River intrusions.

Moreover, the high DIC concentrations observed in Rhône River waters ( $2995 \pm 575 \mu\text{M}$  on average, Sempere et al., 2000) could also affect  $p\text{CO}_2$  variations by increasing the nDIC contribution during intrusion events which counteract the overall decrease of  $p\text{CO}_2$  that is typically observed during these events.

#### 4.2.2 Summer upwelling period (SUP)

During the SUP, regardless of whether there is an LSE,  $p\text{CO}_2$  variations mostly depend on temperature and nDIC which tend to produce anomalies of opposite signs (Fig. 6d). Temperature was highly variable during the SUP due to the succession of upwelling events which explains its significant contribution to  $p\text{CO}_2$  variations. nDIC contribution can be defined as the sum of aeration and biological processes contributions. During the SUP, biological processes represent 29 % of DIC variations (with 14 % attributed to primary production and 15 % to respiration; results not shown). The remaining 71 % are contributions by aeration. While the contribution of aeration decreased during summer, this decrease was compensated by a 9 % increase in the contribution by biological processes (Fig. 6e). The maximum negative anomaly generated by biological processes occurred at the beginning of the SUP, on 31 May (Fig. 6e), evidence that biological processes and more precisely autotrophic processes are enhanced during late spring. This feature is explained by the change in organisms' limitations. At the end of spring, organisms are less limited by temperature and light. Nevertheless, the overall contribution of biological processes was low compared to aeration and temperature ones. This agrees with observations by Wimart-Rousseau et al. (2020) and Lajaunie-Salla et al. (2021) who showed that,  $p\text{CO}_2$  variations and associated  $\text{CO}_2$  fluxes are mostly driven by temperature in the BoM.

We showed that upwelling events were associated with strong decreases in  $p\text{CO}_2$  (Fig. 6c) mostly as a result of temperature changes. The associated decrease in temperature further decreased  $p\text{CO}_2$ . This feature is only observed during upwelling events in summer when both temperatures and  $p\text{CO}_2$  are high (Figs. 6a,c), stressing the importance of upwelling events for these variables. During upwelling events, aeration-generated anomalies change sign and become positive (Fig. 6e). The observed decrease in temperature resulted in a decrease in seawater  $p\text{CO}_2$  to below atmospheric levels, thereby facilitating

a mis en forme : Police :Italique

a mis en forme : Indice

the absorption of atmospheric CO<sub>2</sub> which caused the reversal sign of aeration-generated anomaly. During upwelling events, the contribution by biological processes is low compared to temperature and aeration which both varied significantly (Fig. 6e). While upwelling events only occur at very specific locations (Côte Bleue and Calanques de Marseille, Fig. 4) in our study area, they impact the temperature of the entire BoM (Pairaud et al., 2011). Although upwelling events also bring nutrients and DIC to the surface, these effects are not represented in the Eco3M\_MIX-CarbOx model. We can therefore only assume that the nutrient inputs by promoting primary production (Frayse et al., 2013), would increase the contribution of biological processes (especially of autotrophic processes) resulting in a stronger decrease in *p*CO<sub>2</sub>. However, while DIC inputs would increase the importance of nDIC thereby reducing the decrease of *p*CO<sub>2</sub> associated with these events.

#### 4.3 Air-sea CO<sub>2</sub> fluxes

We have shown that air-sea CO<sub>2</sub> fluxes oscillated between -13 and 15 mmol m<sup>-2</sup> per day (Fig. 5d) which is a range similar to the one obtained by Wimart-Rousseau et al. (2020) (-15 and 10 mmol m<sup>-2</sup> per day) suggesting that our model correctly represents the range of variations of air-sea CO<sub>2</sub> daily fluxes values during the year. CO<sub>2</sub> sinks associated to upwelling events (Lajaunie-Salla et al., 2021) are reproduced by our model. By calculating the daily mean value of air-sea CO<sub>2</sub> fluxes during the SUP, we obtained a positive value of 0.15 mmol m<sup>-2</sup> per day (or 24.2 mmol m<sup>-2</sup> for the entire SUP). To examine this result in more detail, we performed a sensitivity analysis of our air-sea CO<sub>2</sub> flux calculation (see Appendix EC for details) which allowed us to identify the contributions of all relevant parameters (Table 5).

**Table 5. Results of the sensitivity analysis showing the effect of varying the relevant parameters by 10%.**

	Temperature		Salinity		Wind speed		<i>p</i> CO <sub>2</sub> difference	
	+10 %	-10 %	+10 %	-10 %	+10 %	-10 %	+10 %	-10 %
<b>Air-sea CO<sub>2</sub> flux difference (mmol m<sup>-2</sup> d<sup>-1</sup>)</b>	0.016	-0.017	0.044	-0.045	-0.440	0.398	-0.210	0.210

On average, air-sea CO<sub>2</sub> fluxes values during the SUP were mostly driven by wind speed term followed by sea-air *p*CO<sub>2</sub> difference, salinity and finally temperature. According to Eq. (5), wind speed, salinity, and temperature only affect the magnitude of air-sea CO<sub>2</sub> fluxes while their sign is determined by the sea-air *p*CO<sub>2</sub> difference which also impacts their magnitude significantly (Table 5). We have shown that, during the SUP, this difference is mostly driven by temperature since seawater *p*CO<sub>2</sub> variations are controlled by temperature at this time (Figs. 6d,e). A realistic representation of seawater *p*CO<sub>2</sub> is crucial to calculate air-sea CO<sub>2</sub> fluxes. Since seawater *p*CO<sub>2</sub> variations were correctly represented by the model during the SUP (Fig. 4c), the modelled air-sea CO<sub>2</sub> fluxes during the SUP should be reliable.

Over the entire year, air-sea CO<sub>2</sub> fluxes in the BoM essentially evened out yielding only a slightly negative balance of -0.21 mmol m<sup>-2</sup> per year. This is much lower than the -803 mmol m<sup>-2</sup> per year suggested by Wimart-Rousseau et al. (2020). The reason for this discrepancy may be related to the fact that our model overestimates seawater *p*CO<sub>2</sub> during winter, resulting

**inyielding** a sea-air difference close to zero (Fig. 5d). As a result, despite strong winds and low temperatures which would favour CO<sub>2</sub> absorption (Middelburg, 2019), the winter CO<sub>2</sub> sink is not well represented.

Seawater *p*CO<sub>2</sub>, air-sea CO<sub>2</sub> fluxes and DIC are closely connected (Appendix B, Fig. 3-Fig-3). In Eco3M\_MIX-CarbOx, aeration is simulated by applying Eq. (5) to 1 m<sup>3</sup> of surface water at SOLEMIO station which tends to overestimate the impact of aeration process on DIC and, due to the close link between DIC and *p*CO<sub>2</sub>, also on *p*CO<sub>2</sub>. A simple solution to overcome this problem would be to increase the volume in which aeration process is simulated. However, to be consistent with the representation of other fluxes and the dimensionless concept, increasing the volume would require switching from a 0D to a 1D model minimum, which is planned for our future work.

Most studies that investigated air-sea CO<sub>2</sub> fluxes and other carbonate system variables in various Mediterranean locations at different locations (Ligurian Sea, North Adriatic Sea, BoM) were based on measurements only and concluded that their study areas acted as CO<sub>2</sub> sinks during their study periods (e.g., Begovic, 2003; De Carlo et al., 2013; Ingrosso et al., 2016; Urbini et al., 2020; Wimart-Rousseau et al., 2020). To the best of our knowledge, the only other study examining air-sea CO<sub>2</sub> fluxes in the BoM using a modelling approach was conducted by Lajaunie-Salla et al. (2021) using Eco3m-CarbOx model, which is also dimensionless and based on a 1 m<sup>3</sup> volume like Eco3M\_MIX-CarbOx and therefore also tend to underestimate the yearly fluxes. Most modelling studies have focussed on larger scales and employed at least 1D models. For instance, D'Ortenzio et al. (2008), used a coupled 1D model, and found that the Mediterranean Sea, as a whole, was nearly balanced as the western and eastern basins act as CO<sub>2</sub> sink and a source, respectively, and therefore cancel each other out. Using a 3D coupled model and looking at even larger scales, Bourgeois et al. (2016) provided a complete analysis of the air-sea CO<sub>2</sub> fluxes in various coastal environments and have shown that they represent 4.5 % of the anthropogenic CO<sub>2</sub> uptake of the global ocean. 3D models typically allow more realistic representations of the water column, they would allow us to (i) consider a more realistic water volume to perform our air-sea CO<sub>2</sub> fluxes calculation, (ii) consider autochthonous and allochthonous contributions to TA variations, (iii) consider the effects of nutrients and DIC inputs from the Rhône River intrusions and local upwellings. Nevertheless, dimensionless model also offers some advantages such as short simulation time, easy adaptability to as only the forcings need to be modified.

## 5 Conclusion

Using the concept of the dimensionless Eco3M-CarbOx biogeochemical model as a starting point, we developed a new planktonic ecosystem model which contains, in addition to mixotroph organisms, a modified version of the carbonate module described by Lajaunie-Salla et al. (2021), to represent the carbonate system variables more realistically. First, we improved the parametrisation of TA by developing two different formulations: (i) an autochthonous formulation that only considers biological contributions to TA variations and (ii) an allochthonous formulation that only depends on salinity, thus considers riverine contributions to TA variations. A comparison of both TA formulations showed that TA variations in the BoM were mostly due to allochthonous contributions. Then, we adapted the allochthonous formulation for modelling TA

695 variations in the BoM which, yielded a helpful tool to complement the low frequency in situ measurements. We use this new  
formulation to study air-sea CO<sub>2</sub> fluxes and seawater pCO<sub>2</sub> variations at SOLEMIO station in 2017, focussing on two  
hydrodynamic processes that are typical for the BoM: (i) Rhône River intrusions and (ii) summer upwelling events.

700 During the SUP, our model represented the CO<sub>2</sub> sinks generated by summer upwelling events which are suggested by  
Lajaunie-Salla et al., (2021), and identified the underlying drivers of CO<sub>2</sub> variability. Furthermore, our model was able to  
simulate the expected decrease in pCO<sub>2</sub> associated with summer upwelling events (Lajaunie-Salla et al., 2021). This decrease  
was mainly generated by temperature effects on pCO<sub>2</sub>. LSE were also represented by the model. They often generated a  
705 decrease in pCO<sub>2</sub> as a result of the decreasing salinity and increasing TA, especially when those two contributions were not  
counterbalanced by temperature effects. However, in winter, the model was unable to reproduce the undersaturation seen in  
seawater pCO<sub>2</sub> measurements at SOLEMIO station and rather overestimate it. As a result, the commonly observed  
seasonality of air-sea CO<sub>2</sub> fluxes in the north-western Mediterranean was not reproduced by our model which directly  
710 impacted our estimates of the overall yearly air-sea CO<sub>2</sub> flux. While correctly identifying the BoM as an overall sink of CO<sub>2</sub>,  
our model significantly underestimated the magnitude (our model : -0.21 mmol m<sup>-2</sup> per year, Wimart-Rousseau et al., (2020):  
-803 mmol m<sup>-2</sup> per year).

The present work clearly highlighted the limitations of dimensionless models. Although this type of model possesses some  
advantages that facilitate an improved understanding of complex coastal systems, it has clear limitations when it comes to  
715 the representation of specific processes or variables with obvious impacts on the results. The accuracy could be improved by  
employing a 3D coupled model which would allow us to (i) improve our representation of air-sea CO<sub>2</sub> fluxes by applying  
them to the whole water column, (ii) improve our representation of TA by considering autochthonous and other  
allochthonous sources and (iii) improve our representation of LSE and upwelling events by allowing us to consider the  
inputs of nutrients and DIC.



## Appendix A: State equations processes description

Table A1. Description of state equation processes.

Notation	Process
$Remin_{BACeX}^{NutX}$ NutX $\in$ $\{NH_4^+, PO_4^{3-}\}$ X $\in$ {N, P}	Remineralisation of nutrient X by heterotrophic bacteria
$Upt_{NutX}^{PhyX}$ PhyX $\in$ {PICO <sub>N</sub> , NANO <sub>N</sub> , PICO <sub>P</sub> , NANO <sub>P}} NutX <math>\in</math> <math>\{NO_3^-, NH_4^+, PO_4^{3-}\}</math></sub>	Uptake of nutrient X by phytoplankton
$Upt_{NutX}^{CMX}$ X $\in$ {N, P} NutX $\in$ $\{NO_3^-, NH_4^+, PO_4^{3-}\}$	Uptake of nutrient X by constitutive mixotrophs
$Resp_{DIC}^{ZOOe}$	Zooplankton respiration
$Resp_{DIC}^{PhyE}$ Phy $\in$ {PICO, NANO}	Phytoplankton respiration
$Resp_{DIC}^{MIXe}$ MIX $\in$ {NCM, CM}	Mixotrophs respiration
$BR_{DIC}^{BACe}$	Bacterial respiration
$Photo_{DIC}^{PhyE}$ Phy $\in$ {PICO, NANO}	Phytoplankton photosynthesis
$Photo_{DIC}^{MIXe}$ MIX $\in$ {NCM, CM}	Mixotrophs photosynthesis
$Diss_{DIC}^{CaCO_3}$	CaCO <sub>3</sub> dissolution
$Prec_{DIC}^{CaCO_3}$	CaCO <sub>3</sub> precipitation
$Nitrif_{TX}$	Nitrification
$Aera_{DIC}$	Air-sea CO <sub>2</sub> gas exchanges (aeration)

Notation	Process
$Excl_{NutX}^{COPX}$ NutX $\in$ $\{NH_4^+, PO_4^{3-}\}$ X $\in$ {N, P}	<u>Excretion of nutrient X by copepods</u>
$Excl_{DOC}^{COPC}$	<u>DOC excretion by copepods</u>
$Resp_{DIC}^{COPC}$	<u>Copepods respiration</u>

- a mis en forme : Couleur de police : Automatique
- a mis en forme : Interligne : simple
- a mis en forme : Couleur de police : Automatique
- a mis en forme : Interligne : simple
- a mis en forme : Police : Non Gras, Couleur de police : Automatique
- a mis en forme : Interligne : simple
- a mis en forme : Police : Non Gras, Couleur de police : Automatique
- a mis en forme : Police : Non Gras, Couleur de police : Automatique
- a mis en forme : Interligne : simple
- a mis en forme : Police : Non Gras, Couleur de police : Automatique
- a mis en forme : Interligne : simple

$E_{POX}^{COPX}$   
 $X \in [C, N, P]$

Copepods egestion

Predation $_{POX}^{COPX}$   
 $X \in [C, N, P]$

Predation by higher trophic levels on copepods

### Mixotrophs (Mix $\in$ [NCM, CM])

Exu $_{DOX}^{MixX_i}$   
 $X \in [C, N, P]$

DOX exudation by mixotrophs

Resp $_{DIC}^{MixC}$

Mixotrophs respiration

Photo $_{DIC}^{MixC}$

Mixotrophs photosynthesis

Exc $_{NutX}^{NCMX}$   
NutX  $\in [NH_4^+, PO_4^{3-}]$   
 $X \in [N, P]$

Excretion of nutrient X by NCM

Upt $_{NutX}^{CMX}$   
 $X \in [N, P]$   
NutX  $\in [NO_3^-, NH_4^+, PO_4^{3-}]$

Uptake of nutrient X by constitutive mixotrophs

Upt $_{DOX}^{CMX}$   
 $X \in [N, P]$

Uptake of DOX by constitutive mixotrophs

### Phytoplankton (Phy $\in$ [NMPHYTO, PICOL])

Resp $_{DIC}^{PhyC}$

Phytoplankton respiration

Photo $_{DIC}^{PhyC}$

Phytoplankton photosynthesis

Upt $_{NutX}^{PhyX}$   
NutX  $\in [NO_3^-, NH_4^+, PO_4^{3-}]$

Uptake of nutrient X by phytoplankton

Exu $_{DOX}^{PhyX}$   
 $X \in [C, N, P]$

DOX exudation by phytoplankton

Upt $_{DOX}^{PICOX}$   
 $X \in [N, P]$

Uptake of DOX by picophytoplankton

### Heterotrophic bacteria

Br $_X^{BACC}$   
 $X \in [DOC, POC]$

Bacterial production

Br $_{DIC}^{BACC}$

Bacterial respiration

Upt $_{POX}^{BACX}$   
 $X \in [N, P]$

POX uptake by heterotrophic bacteria

Exu $_{DOX}^{PhyX_i}$   
 $X \in [C, N, P]$

DOX exudation by phytoplankton

Remin $_{BACX}^{NutX}$   
NutX  $\in [NH_4^+, PO_4^{3-}]$   
 $X \in [N, P]$

Remineralisation of nutrient X by heterotrophic bacteria

a mis en forme

a mis en forme

a mis en forme

a mis en forme

a mis en forme

a mis en forme

a mis en forme

a mis en forme

a mis en forme

a mis en forme

a mis en forme

a mis en forme

a mis en forme

a mis en forme

a mis en forme

a mis en forme

a mis en forme

a mis en forme

a mis en forme

a mis en forme

a mis en forme

a mis en forme

a mis en forme

a mis en forme

a mis en forme

a mis en forme

a mis en forme

a mis en forme

a mis en forme

a mis en forme

a mis en forme

a mis en forme

a mis en forme

a mis en forme

a mis en forme

a mis en forme

a mis en forme

a mis en forme

a mis en forme

a mis en forme

a mis en forme

a mis en forme

a mis en forme

a mis en forme

a mis en forme

a mis en forme

Mort<sup>BACx</sup><sub>DOX</sub> ▲ Heterotrophic bacteria natural mortality

Dissolved inorganic matter (DIM)

Diss<sup>CaCO<sub>3</sub></sup><sub>DIC</sub> ▲ CaCO<sub>3</sub> dissolution

Prec<sup>CaCO<sub>3</sub></sup><sub>DIC</sub> ▲ CaCO<sub>3</sub> precipitation

Nitri<sup>f</sup> ▲ Nitrification

Aera<sup>DIC</sup> ▲ Air-sea CO<sub>2</sub> gas exchanges (aeration)

**a mis en forme** : Police :Non Gras, Couleur de police : Automatique

**a mis en forme** : Police :Non Gras

**a mis en forme** : Interligne : simple

**a mis en forme** : Couleur de police : Automatique

**a mis en forme** : Interligne : simple

**a mis en forme** : Police :Non Gras, Couleur de police : Automatique

**a mis en forme** : Interligne : simple

**a mis en forme** : Police :Non Gras, Couleur de police : Automatique

**a mis en forme** : Interligne : simple

**a mis en forme** : Police :Non Gras, Couleur de police : Automatique

**a mis en forme** : Interligne : simple

**a mis en forme** : Police :Non Gras, Couleur de police : Automatique

**a mis en forme** : Interligne : simple

720 **Appendix B: pH<sub>T</sub> and pCO<sub>2</sub> calculation**

The calculation method performed in the Eco3M\_MIX-CarbOx model to obtain pH<sub>T</sub> and pCO<sub>2</sub> is detailed below. As specified in Sect. 2, we used the method introduced by Lajaunie-Salla et al. (2021), which is based on CO2SYSv3 (Sharp et al., 2020), a software originally developed by Lewis and Wallas (1998) to perform the resolution of carbonate system, to perform this calculation. This appendix aims to complete Appendix A from Lajaunie-Salla et al. (2021) by providing some corrections.

**B.1 Equilibrium constants and conservative elements concentrations calculation**

In the following formulations, *S* represents the practical salinity.

**B.1.1 Conservative elements concentrations and ionic strength**

**Table B1. Formulations of conservative elements concentrations and ionic strength.**

Description	Formulation	Units
Concentration in total fluoride (Riley, 1965)	$TF = \frac{0.000067}{18.998} * \frac{S}{1.80655}$	mol kg <sup>-1</sup>
Concentration in total sulfate (Morris & Riley, 1966)	$TS = \frac{0.14}{96.062} * \frac{S}{1.80655}$	mol kg <sup>-1</sup>
Concentration in total Boron (Uppström, 1974)	$TB = \frac{0.000416 * S}{35}$	mol kg <sup>-1</sup>
Concentration in calcium ion (Riley & Tongudai, 1967)	$Ca^{2+} = \frac{0.02128}{40.087} * \frac{S}{1.80655}$	mol kg <sup>-1</sup>
Ionic strength (DOE, 1994)	$IonS = \frac{19.924 * S}{1000 - 1.005 * S}$	∅

730 **B.1.2 Equilibrium constants**

In the following formulations, *T* represents temperature value converted in Kelvin (i.e., T(°C) + 273.15).

K<sub>F</sub> (mol kg<sup>-1</sup>): HF dissociation constant (Dickson & Riley, 1979)

$$\ln(K_F) = \frac{1590.2}{T} - 12.641 + 1.525 * IonS^{0.5}$$

$$K_F = \exp(\ln(K_F) * (1 - 0.001005 * S))$$

(B1)

735 K<sub>F</sub> is expressed on free pH scale.

$K_S$  (mol kg<sup>-1</sup>): HSO<sub>4</sub><sup>-</sup> dissociation constant (Dickson, 1990a)

$$\begin{aligned} \ln(K_S)_{temp} &= -\frac{4276.1}{T} + 141.328 - 23.093 * \ln(T) + \left(-\frac{13856}{T} + 324.57 - 47.986 * \ln(T)\right) * IonS^{0.5} \\ \ln(K_S) &= \ln(K_S)_{temp} + \left(\frac{35474}{T} - 771.54 + 114,723 * \ln(T)\right) * IonS - \frac{2698}{T} * IonS^{1.5} + \frac{1776}{T} * IonS^2 \\ K_S &= \exp(\ln(K_S) * (1 - 0.001005 * S)) \end{aligned} \quad (B2)$$

740  $K_S$  is expressed on free pH scale.

$K_B$  (mol kg<sup>-1</sup>): B(OH)<sub>3</sub> dissociation constant (Dickson, 1990b)

$$\begin{aligned} \ln(K_B)_{temp} &= \frac{-8996.9 - 2890.53 * S^{0.5} - 77.942 * S + 1.728 * S^{1.5} - 0.0996 * S^2}{T} + 148.0248 + 137.1942 * S^{0.5} \\ \ln(K_B) &= \ln(K_B)_{temp} + 1.62142 * S + (-24.4344 - 25.085 * S^{0.5} - 0.2474 * S) * \ln(T) + 0.053105 * S^{0.5} * T \\ K_B &= \exp(\ln(K_B)) \end{aligned} \quad (B3)$$

745  $K_B$  is expressed on total pH scale.

$K_{ca}$  (mol kg<sup>-1</sup>): Calcite formation constant (Mucci, 1983)

$$\begin{aligned} \log(K_{ca})_{temp} &= -171.9065 - 0.077993 * T + \frac{2839.319}{T} + 71.595 * \log(T) \\ \log(K_{ca}) &= \log(K_{ca})_{temp} + \left(-0.77712 + 0.0028426 * T + \frac{178.34}{T}\right) * S^{0.5} - 0.07711 * S + 0.0041249 * S^{1.5} \\ K_{ca} &= 10^{(\log(K_{ca}))} \end{aligned} \quad (B4)$$

750  $K_e$  (mol kg<sup>-1</sup>): H<sub>2</sub>O dissociation constant (Millero, 1995)

$$\begin{aligned} \ln(K_e) &= -\frac{13847.26}{T} + 148.9802 - 23.6521 * \ln(T) + \left(-5.977 + \frac{118.67}{T} + 1.0495 * \ln(T)\right) * S^{0.5} - 0.01615 * S \\ K_e &= \exp(\ln(K_e)) \end{aligned} \quad (B5)$$

$K_e$  is expressed on SWS pH scale.

$K_0$  (mol kg<sup>-1</sup> atm<sup>-1</sup>): CO<sub>2</sub> solubility (Weiss, 1974)

$$\begin{aligned} \ln(K_0)_{temp} &= -60.2409 + 93.4517 * \frac{100}{T} + 23.3585 * \ln\left(\frac{T}{100}\right) \\ \ln(K_0) &= \ln(K_0)_{temp} + S * \left(0.023517 - 0.023656 * \frac{T}{100} + 0.0047036 * \left(\frac{T}{100}\right)^2\right) \\ K_0 &= \exp(\ln(K_0)) \end{aligned} \quad (B6)$$

$K_1$  (mol kg<sup>-1</sup>): H<sub>2</sub>CO<sub>3</sub> dissociation (Lueker et al., 2000)

$$\begin{aligned} pK_1 &= \frac{3633.86}{T} - 61.2172 + 9.6777 * \ln(T) - 0.011555 * S + 0.0001152 * S^2 \\ K_1 &= 10^{(-pK_1)} \end{aligned} \quad (B7)$$

$K_1$  is expressed on total pH scale.

$K_2$  (mol kg<sup>-1</sup>): HCO<sub>3</sub><sup>-</sup> dissociation (Lueker et al., 2000)

$$pK_2 = \frac{471.78}{T} + 25.929 - 3.16967 * \ln(T) - 0.01781 * S + 0.0001122 * S^2$$

$$K_2 = 10^{(-pK_2)}$$

(B8)

765  $K_2$  is expressed on total pH scale.

### B.1.3 pH scale conversion

pH calculation is performed on total scale. Accordingly, the previous constants are converted if necessary (i.e., expressed on total pH scale) using the following conversion factors. Except  $K_S$  and  $K_F$  which must be expressed on free pH scale, the other equilibrium constants must be converted to total pH scale.

770 **Table B2. Formulation of pH scale conversion factors.**

Description	Conversion factor
From SWS pH scale to total pH scale	$\frac{1 + \frac{T_S}{K_S}}{1 + \frac{T_S}{K_S} + \frac{T_F}{K_F}}$
From free pH scale to total pH scale	$1 + \frac{T_S}{K_S}$

### B.1.4 Pressure correction

All the constants are corrected by the effect of hydrostatic pressure using the following formulations (Millero, 1995). We define  $T_K$  and  $T_C$  which represents respectively the temperature in Kelvin and in Celsius degree. R represents the gas constant in ml bar<sup>-1</sup> K<sup>-1</sup> mol<sup>-1</sup> (R = 83.1451 ml bar<sup>-1</sup> K<sup>-1</sup> mol<sup>-1</sup>) and P the pressure in bar.

775 Corrected  $K_F$  (mol kg<sup>-1</sup>):

$$K_F CorrFac = \frac{(9.78 + 0.009 * T_C + 0.0009429 * T_C^2 + 0.5 * (\frac{-3.91 + 0.054 * T_C}{1000}) * P) * P}{R * T_K}$$

$$K_F = K_F * \exp(K_F CorrFac)$$

(B9)

Corrected  $K_S$  (mol kg<sup>-1</sup>):

$$K_S CorrFac = \frac{(18.03 - 0.0466 * T_C - 0.000316 * T_C^2 + 0.5 * (\frac{-4.53 + 0.09 * T_C}{1000}) * P) * P}{R * T_K}$$

780  $K_S = K_S * \exp(K_S CorrFac)$

(B10)

Corrected  $K_B$  (mol kg<sup>-1</sup>):

$$K_B \text{CorrFac} = \frac{(29.48 - 0.1622 \cdot T_C + 0.002608 \cdot T_C^2 + 0.5 \cdot (\frac{2.84}{1000}) \cdot P) \cdot P}{R \cdot T_K}$$

$$K_B = K_B \cdot \exp(K_B \text{CorrFac}) \quad (\text{B11})$$

Corrected  $K_{ca}$  (mol kg<sup>-1</sup>):

$$785 \quad K_{ca} \text{CorrFac} = \frac{(48.76 - 0.5304 \cdot T_C + 0.5 \cdot (\frac{-11.76 + 0.3692 \cdot T_C}{1000}) \cdot P) \cdot P}{R \cdot T_K}$$

$$K_{ca} = K_{ca} \cdot \exp(K_{ca} \text{CorrFac}) \quad (\text{B12})$$

Corrected  $K_e$  (mol kg<sup>-1</sup>):

$$K_e \text{CorrFac} = \frac{(20.02 - 0.1119 \cdot T_C + 0.001409 \cdot T_C^2 + 0.5 \cdot (\frac{-5.13 + 0.0794 \cdot T_C}{1000}) \cdot P) \cdot P}{R \cdot T_K}$$

$$K_e \text{CorrFac} = K_e \cdot \exp(K_e \text{CorrFac}) \quad (\text{B13})$$

790 Corrected  $K_1$  (mol kg<sup>-1</sup>):

$$K_1 \text{CorrFac} = \frac{(25.5 - 0.1271 \cdot T_C + 0.5 \cdot (\frac{-3.08 + 0.0877 \cdot T_C}{1000}) \cdot P) \cdot P}{R \cdot T_K}$$

$$K_1 = K_1 \cdot \exp(K_1 \text{CorrFac}) \quad (\text{B14})$$

Corrected  $K_2$  (mol kg<sup>-1</sup>):

$$795 \quad K_2 \text{CorrFac} = \frac{(15.82 + 0.0219 \cdot T_C + 0.5 \cdot (\frac{1.13 + 0.1475 \cdot T_C}{1000}) \cdot P) \cdot P}{R \cdot T_K}$$

$$K_2 = K_2 \cdot \exp(K_2 \text{CorrFac}) \quad (\text{B15})$$

### B.1.5 Fugacity factor

To perform the calculation of the fugacity factor (FugFac), we supposed that the pressure value is close or equal to an atmosphere (Weiss, 1974).

T represents the temperature in Kelvin. We define  $P_{atm}$ , as the atmospheric pressure in bar:  $P_{atm} = 1.01325$  bar.

$$800 \quad \ln(\text{FugFac}) = \frac{((-1636.75 + 12.0408 \cdot T - 0.0327957 \cdot T^2 + 3.16528 \cdot 0.00001 \cdot T^3) + 2 \cdot (57.7 - 0.118 \cdot T)) \cdot P_{atm}}{R \cdot T}$$

$$\text{FugFac} = \exp(\ln(\text{FugFac})) \quad (\text{B16})$$

## B.2 pH<sub>T</sub> and pCO<sub>2</sub> calculation

### B.2.1 pH<sub>T</sub> calculation

805 As specified in Sect. 2, we obtain the new pH<sub>T</sub> value using the buffering value (B). B is defined as the pH variation induced by an addition of acid or base to a considered solution (Van Slycke, 1922). In seawater, the expression of buffering value is based on TA (Middelburg, 2019), the pH<sub>T</sub> variation is then, calculated as follows:

$$B = \frac{\partial TA}{\partial pH_T} \Leftrightarrow \Delta pH_T = \frac{\partial TA}{\sum_{i=1}^n B_i}, \quad (\text{B17})$$

where *i* represents a chemical species contributing to TA.

810 Accordingly, we calculate the pH<sub>T</sub> difference between two model time steps ( $\Delta pH_T$ ) using an iterative method. We set the pH<sub>T</sub> initial value to 8.0. We chose this value by considering the Mediterranean and Rhône River pH<sub>T</sub> which are respectively close and equal to 8.0. Finally, considering that the measurements precision is rather close to 0.0004 (Clayton & Byrne, 1993), we set the tolerance threshold to 0.0001. pH<sub>T</sub> calculation is detailed below:

```
! pH initial value = 8.0
! pHtol = Tolerance threshold --> 0.0001
! deltaph = pH difference between two model iterations
! pH is calculated on total scale

if (nbIter < 1) pH = 8.0

pHTol = 0.0001
deltaph = pHTol + 1

do while (abs(deltaph) > pHTol)
  H = 10^(-pH)
  Denom = H^2 + K1 * H + K1 * K2
  CALk = DIC * K1 * ((H + 2 * K2)/Denom) !Carbonate Alkalinity
  BAlk = (TB * KB)/(KB + H) ! Borate Alkalinity
  OH = Ke/H
  FreeToTot = 1 + (TS/KS)
  HFree = H/FreeToTot
  HSO4 = TS/(1+(KS/HFree))
  HF = TF/(1+(KF/H))
  Residual = TA - CALk - BAlk - OH + HFree + HSO4 + HF
  Slope = DIC * H * K1 * (H^2 + K1 * K2 + 4 * H * K2)
  Slope = Slope/(Denom^2) + OH + H + (BAlk * H)/(KB + H)
  Slope = log(10) * Slope
  deltaph = Residual/Slope

  do while (abs(deltaph) > 1)
    deltaph = deltaph/2
  enddo

pH = pH + deltaph
enddo
```

815 **Figure B1: pH<sub>T</sub> calculation**



### B.2.2 $p\text{CO}_2$ and carbonate system species concentrations

$p\text{CO}_2$  is deducted using DIC, pH (via  $\text{H}^+$  concentration) and equilibrium constants. We also calculate the concentrations of  $\text{CO}_2$ ,  $\text{HCO}_3^-$ ,  $\text{CO}_3^{2-}$  and  $\text{CaCO}_3$  saturation ( $\Omega$ ).

**Table B3. Formulation of  $p\text{CO}_2$  and carbon system species concentrations.**

Description	Formulation	Units
$p\text{CO}_2$	$p\text{CO}_2 = \frac{\text{DIC} * [\text{H}^+]^2}{[\text{H}^+]^2 + K_1 * [\text{H}^+] + K_1 * K_2} * \frac{10^6}{K_0 * \text{FugFac}}$	$\mu\text{atm}$
$\text{CO}_2$ concentration	$[\text{CO}_2] = \frac{(\text{DIC} * 10^6)}{\left(1 + \frac{K_1}{[\text{H}^+]} + \frac{K_1 * K_2}{[\text{H}^+]^2}\right)}$	$\mu\text{mol kg}^{-1}$
$\text{HCO}_3^-$ concentration	$[\text{HCO}_3^-] = \frac{K_1 * [\text{CO}_2]}{[\text{H}^+]}$	$\mu\text{mol kg}^{-1}$
$\text{CO}_3^{2-}$ concentration	$[\text{CO}_3^{2-}] = \frac{K_2 * [\text{HCO}_3^-]}{[\text{H}^+]}$	$\mu\text{mol kg}^{-1}$
$\text{CaCO}_3$ saturation state	$\Omega = \frac{[\text{Ca}^{2+}] * [\text{CO}_3^{2-}] * 10^{-6}}{K_{ca}}$	$\emptyset$

**Appendix C: Statistic indicators calculation for H<sup>+</sup> concentration**

**Table C1: Comparing the different model results to surface observations at SOLEMIO station for H<sup>+</sup> concentration. N represents the number of observations. Mean, SD, AE, AAE and RMSD are in the same unit than the considered variable, i.e.: mmol m<sup>-3</sup> for H<sup>+</sup> concentrations. % BIAS is without unit.**

		<b>[H<sup>+</sup>]</b>
<b><u>N</u></b>	Observations	20
<b><u>Mean ± SD</u></b>	Observations	$8.08 \times 10^{-9} \pm 5.52 \times 10^{-10}$
<b><u>Mean ± SD</u></b>	SIMC0	$8.89 \times 10^{-9} \pm 2.91 \times 10^{-10}$
	SIMC1	$8.39 \times 10^{-9} \pm 4.06 \times 10^{-10}$
	CarbOx	$8.52 \times 10^{-9} \pm 2.80 \times 10^{-10}$
<b><u>%BIAS</u></b>	SIMC0	-5.33
	SIMC1	-3.91
	CarbOx	-5.47
<b><u>AE</u></b>	SIMC0	$-4.30 \times 10^{-10}$
	SIMC1	$-3.15 \times 10^{-10}$
	CarbOx	$-4.42 \times 10^{-10}$
<b><u>AAE</u></b>	SIMC0	$6.45 \times 10^{-10}$
	SIMC1	$6.05 \times 10^{-10}$
	CarbOx	$6.36 \times 10^{-10}$
<b><u>RMSD</u></b>	SIMC0	$6.98 \times 10^{-10}$
	SIMC1	$7.14 \times 10^{-10}$
	CarbOx	$6.93 \times 10^{-10}$

a mis en forme : Expositant

a mis en forme : Couleur de police : Automatique, Expositant

a mis en forme : Légende

a mis en forme : Couleur de police : Automatique, Expositant

a mis en forme : Police :

a mis en forme : Expositant

a mis en forme : Interligne : simple

a mis en forme : Interligne : simple

a mis en forme : Interligne : simple

a mis en forme : Interligne : simple

a mis en forme : Interligne : simple

a mis en forme : Interligne : simple

a mis en forme : Interligne : simple

a mis en forme : Interligne : simple

825

**Appendix D: Time series of daily average  $p\text{CO}_2$  anomalies generated by DIC, TA, Fw+S and temperature based on the approach described in Lovenduski et al. (2007), for 2017. Enlargement of the panel d of figure 6.**

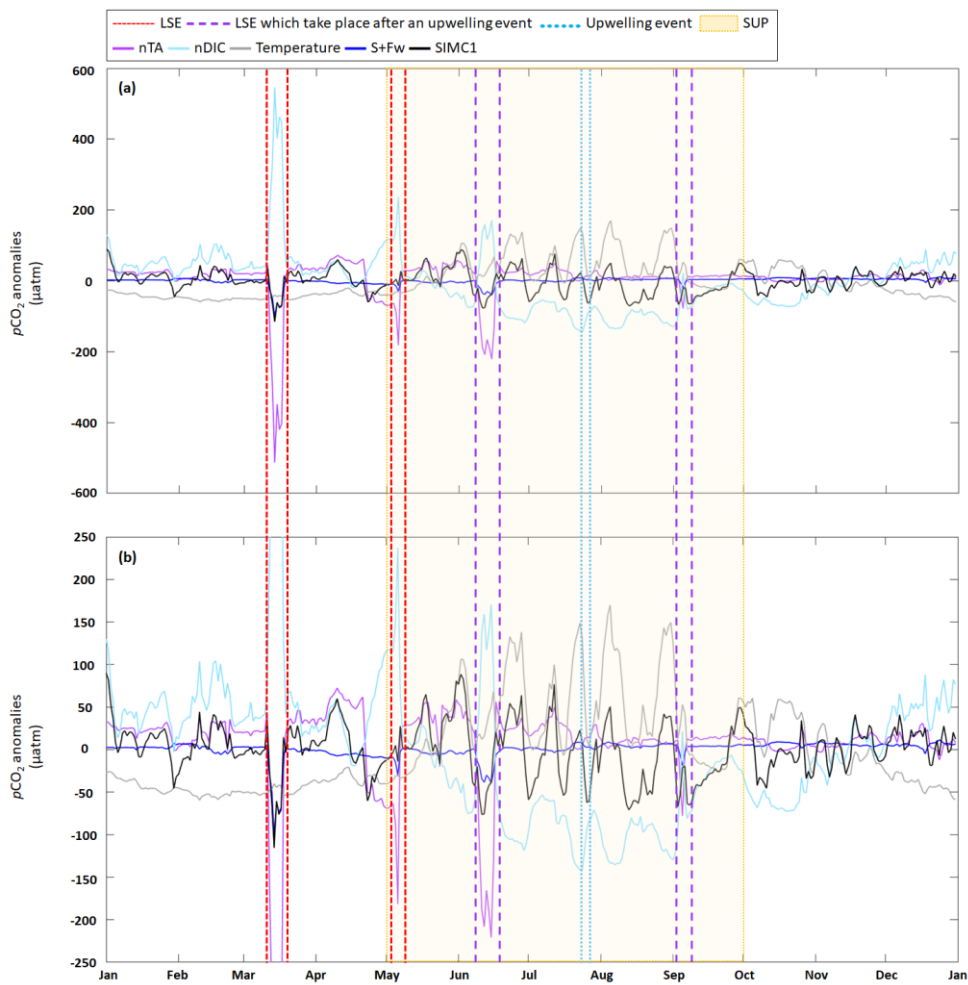


**Figure D1. Time series for 2017 of daily average (a)  $p\text{CO}_2$  anomalies generated by DIC, TA, Fw+S and temperature based on the approach in Lovenduski et al. (2007) (Note: the dark blue line is sometimes obscured by the black line, especially in March), (b)**

a mis en forme : Police :Italique

a mis en forme : Indice

a mis en forme : Titre 1

a mis en forme : Police :Italique

a mis en forme : Indice

a mis en forme : Légende

Enlargement of the panel a between -250 and 250  $\mu\text{atm}$ . LSE and an upwelling event have been highlighted. The summer upwelling period (SUP) is indicated by yellow shading.

835 **Appendix CE: Sensibility analysis performed on air-sea CO<sub>2</sub> fluxes calculation.**

A sensibility analysis was performed to evaluate the importance of temperature, salinity, wind speed and seawater-atmospheric pCO<sub>2</sub> difference terms in the air-sea CO<sub>2</sub> fluxes calculation. Previous terms are one by one increased (decreased) by 10 %. Air-sea CO<sub>2</sub> fluxes are then, post-processed using the Eqs. (85) and (96). Calculation is performed using MATLAB. We present in Table 5 the mean difference between the reference air-sea CO<sub>2</sub> fluxes (i.e., calculated without increasing (decreasing) by 10 % one of the calculation terms) and the air-sea CO<sub>2</sub> fluxes obtained by adding (removing) 10 % to one of the terms of the calculation (Eq. CE1).

$$\Delta_{\text{Air-seaCO}_2\text{Fluxes}} = \frac{1}{N} * \sum_{i=1}^N (\text{abs}(\text{Ref}) - \text{abs}(X_{10\%})),$$

(CE1)

a mis en forme : Droite

where  $\Delta_{\text{Air-seaCO}_2\text{Fluxes}}$  is expressed in mmol m<sup>-2</sup> s<sup>-1</sup> N is the number of modelled values. X represents temperature, salinity, wind speed or the difference between seawater and atmospheric pCO<sub>2</sub>

845

### Code availability

The current version of Eco3M\_MIX-CarbOx is available from the Zenodo website ([https://zenodo.org/record/7669658#.Y\\_dAJ0NKg2w](https://zenodo.org/record/7669658#.Y_dAJ0NKg2w), last access: 23 February 2023) under the Creative Commons Attribution 4.0 international licence. The exact version of the model used to produce the results in this paper is archived on Zenodo (Barré Lucille, Diaz Frédéric, Wagener Thibaut, Van Wambeke France, Mazoyer Camille, Yohia Christophe, & Pinazo Christel. (2022). Eco3M\_MIX-CarbOx (v1.0). Zenodo. <https://doi.org/10.5281/zenodo.7669658>), as are input data and scripts to run the model and produce the plots for all the simulation presented in this paper.

### Data availability

SOLEMIO time serie data is available on <https://www.seanoe.org>. Temperature data is available on [www.t-mednet.org](http://www.t-mednet.org) by filling out the request form for station and years pre-selected. Salinity data is available on <https://erddap.osupytheas.fr>. The non-processed atmospheric  $p\text{CO}_2$  data can be found on <https://servicedata.atmosud.org/donnees-stations>. Request for processed atmospheric  $p\text{CO}_2$  data should be addressed to [alexandre.armengaud@airpaca.org](mailto:alexandre.armengaud@airpaca.org) and [irene.xuerefremy@imbe.fr](mailto:irene.xuerefremy@imbe.fr).

### 860 Author contribution

LB conceptualized this study, developed the Eco3M\_MIX-CarbOx model v1.0, and it, designed the numerical experiments, developed MATLAB software to visualize and process the model results, processed, and analysed the model results, wrote the initial draft. FD provided the initial version of the model code (without carbonate module and with an initial implementation of the mixotroph organisms) and helped to develop the Eco3M\_MIX-CarbOx v1.0. TW participated to the conceptualization of this study, participated to the data acquisition of carbonate variables, helped to design the numerical experiments, analysed the model results, reviewed, and edited the initial draft. CM helped in the model development process by giving expertise on the code development to reduce calculation time. CY provided the wind and irradiance data, maintained computing resources. CP acquired the fundings, participated to the conceptualization of this study and supervised it, participated to the model development, designed the numerical experiments, analysed the model results, and reviewed and edited the initial draft.

### Competing interests

The authors declare that they have no conflict of interest.

## Acknowledgements

We thank the National Service d'Observation en MILieu Littoral (SOMLIT) for its permission to use SOLEMIO data. We  
875 would like to thank the crew members of the RV Antedon II, operated by the DT-INSU, for making these samplings  
possible, the team of the SAM platform (Service Atmosphère Mer) of the MIO for help with the field work. We also thank  
Michel Lafont and Véronique Lagadec of the PACEM (Plateforme Analytique de Chimie des Environnements Marins)  
platform of the MIO and the SNAPO-CO<sub>2</sub> at LOCEAN, Paris. The SNAPO-CO<sub>2</sub> service at LOCEAN is supported by  
CNRS-INSU and OSU Ecce-Terra. We acknowledge the TMEDNet team for its permission to use the Planier-Souquet  
880 temperature data. We thank the ROMARIN network team for its permission to use the salinity data from Carry buoy. We  
thank the observatoire de la qualité de l'air en Région Sud Provence-Alpes-Côte d'Azur (ATMOSUD) in particular,  
Alexandre Armengaud, and the AMC (Aix-Marseille Carbon Pilot Study) project leaders, Irène Xueref-Remy and  
Dominique Lefèvre for providing the atmospheric CO<sub>2</sub> data at the Cinq Avenue station. We acknowledge the staff of the  
"Cluster de calcul intensif HPC" platform of the OSU Institut PYTHEAS (Aix-Marseille Université, INSU-CNRS) for  
885 providing the computing facilities. We would like to thank Julien Lecubin from the Service Informatique de l'OSU Institut  
Pytheas for its technical assistance. We thank XpertScientific team for the manuscript correction.

## Fundings

This work takes part of the IAMM project (Évaluer l'Impact de la métropole Aix-Marseille sur l'Acidification de la baie de  
Marseille et les conséquences sur les microorganismes marins, approche par Modélisation) funded by the public  
890 establishment of the Ministry of the Environment, l'Agence de l'eau Rhône Méditerranée Corse.

## References

- Allen, J. I., Holt, J. T., Blackford, J. and Proctor, R.: Error quantification of a high-resolution coupled  
hydrodynamicecosystem coastal-ocean model: Part 2. Chlorophyll-a, nutrients and SPM, *Journal of Marine Systems*, 68,  
381-404, <https://doi.org/10.1016/j.jmarsys.2007.01.005>, 2007.
- 895 Artioli, Y., Blackford, J. C., Nondal, G., Bellerby, R. J. G., Wakelin, S. L., Holt, J. T., Butenschön, M. and Allen, I. J.:  
Heterogeneity of impacts of high CO<sub>2</sub> on the North-western European Shelf, *Biogeosciences*, 11, 601-612,  
<https://doi.org/10.5194/bg-11-601-2014>, 2014.
- Baklouti, M., Faure, V., Pawlowski, L., and Sciandra, A.: Investigation and sensitivity analysis of a mechanistic  
phytoplankton model implemented in a new modular numerical tool (Eco3M) dedicated to biogeochemical modelling, *Prog.*  
900 *Oceanogr.*, 71, 34-58, <https://doi.org/10.1016/j.pocean.2006.05.003>, 2006a.

Baklouti, M., Diaz, F., Pinazo, C., Faure, V. and Queguiner, B.: Investigation of mechanistic formulations depicting phytoplankton dynamics for models of marine pelagic ecosystems and description of a new model, *Prog. Oceanogr.*, 71, 1-33, <https://doi.org/doi:10.1016/j.poccean.2006.05.002>, 2006b.

905 Barré, L., Diaz, F., Wagener, T., Van Wambeke, F., Mazoyer, C., Yohia, C. and Pinazo, C.: Implementation and assessment of a model including mixotrophs and the carbonate cycle (Eco3M\_MIX-CarbOx v1.0) in a highly dynamic Mediterranean coastal environment (Bay of Marseille, France) (Part I): Evolution of ecosystem composition under limited light and nutrient conditions, *submitted to GMD, 2023*, <https://doi.org/10.5194/gmd-16-6701-2023>, 2023.

Barrier, N., Petrenko, A. A. and Ourmières, Y.: Strong intrusions of the Northern Mediterranean Current on the eastern Gulf of Lion: insights from in-situ observations and high-resolution numerical modelling, *Ocean Dynamics*, 66, 313-327, 910 <https://doi.org/10.1007/s10236-016-0921-7>, 2016.

Bates, N. R., Best, M. H. P., Neely, K., Garley, R., Dickson, A. G. and Johnson, R. J.: Detecting anthropogenic carbon dioxide uptake and ocean acidification in the North Atlantic Ocean, *Biogeosciences*, 9, 2500-2522, <https://doi.org/10.5194/bg-9-2509-2012>, 2012.

Begovic, M.: Contribution à l'étude du système des carbonates en Méditerranée-Distribution et variation spatio-temporelle de la pression partielle de CO<sub>2</sub> dans les eaux superficielles du bassin Liguro-Provençal, Ph.D. Thesis, Université Pierre et Marie Curie - Paris VI, 2001.

915 Bourgeois, T., Orr, J. C., Resplandy, L., Terhaar, J., Ethé, C., Gehlen, M. and Bopp, L.: Coastal-ocean uptake of anthropogenic carbon, *Biogeosciences*, 13, 4167-4185, <https://doi.org/10.5194/bg-13-4167-2016>, 2016.

Brenner, H., Braeckman, U., Le Guitton, M. and Meysman, F. J. R.: The impact of sedimentary alkalinity release on the water column CO<sub>2</sub> system in the North Sea, *Biogeosciences*, 13, 841-863, <https://doi.org/10.5194/bg-13-841-2016>, 2016.

920 Carstensen, J., Chierci, M., Gustafsson, B. G. and Gustafsson, E.: Long-term and seasonal trends in estuarine and coastal carbonate systems, *Global Biogeochemical Cycles*, 32, 497-513, <https://doi.org/10.1002/2017gb005781>, 2018.

Copin-Montegut, C.: Alkalinity and carbon budgets in the Mediterranean Sea, *Global Biogeochemical Cycles*, 7, 915-925, <https://doi.org/10.1029/93GB01826>, 1993.

925 Cossarini, G., Lazzari, P. and Solidoro, C.: Spatiotemporal variability of alkalinity in the Mediterranean Sea, *Biogeosciences*, 12, 1645-1658, <https://doi.org/10.5194/bg-12-1647-2015>, 2015.

Crossland, C. J., Baird, D., Ducrotot, J.-P. and Lindeboom, H. J.: The coastal zone, a domain of global interactions, *Coastal Fluxes in the Anthropocene*, Global Change – The IGBP Series, Springer-Verlag, pp 1-38, 2005.

930 De Carlo, E. H., Mousseau, L., Passafiume, O., Drupp, P. S. and Gattuso, J. -P.: Carbonate Chemistry and Air–Sea CO<sub>2</sub> Flux in a NW Mediterranean Bay Over a Four-Year Period: 2007–2011, *Aquatic Geochemistry*, 19, 399-442, <https://doi.org/10.1007/s10498-013-9217-4>, 2013.

Dickson, A. G.: Standard potential of the reaction: AgCl(s) + 1/2 H<sub>2</sub>(g) = Ag(s) + HCl(aq), and the standard acidity constant of the ion HSO<sub>4</sub><sup>-</sup> in synthetic seawater from 273.15 to 318.15 K, *Journal of Chemical Thermodynamics*, 22, 113-127, 1990a.



- Dickson, A. G.: Thermodynamics of the dissociation of boric acid in synthetic seawater from 273.15 to 318.15 K, *Deep-Sea Research*, 37, 755–766, [https://doi.org/10.1016/0198-0149\(90\)90004-F](https://doi.org/10.1016/0198-0149(90)90004-F), 1990b.
- 935 Dickson, A. G. and Riley, J. P.: The estimation of acid dissociation constants in seawater media from potentiometric titrations with strong base. I. The ionic product of water – KW, *Marine Chemistry*, 7, 89-99, 1979a.
- Dickson, A. G. and Riley, J. P.: The estimation of acid dissociation constants in sea-water media from potentiometric titrations with strong base. II. The dissociation of phosphoric acid, *Marine Chemistry*, 7, 101–109,
- 940 [https://doi.org/10.1016/0304-4203\(79\)90002-1](https://doi.org/10.1016/0304-4203(79)90002-1), 1979b.
- DOE (U.S. Department of Energy): Handbook of methods for the analysis of the various parameters of the carbon dioxide system in seawater; version 2. A.G. Dickson, and C. Goyet, eds. ORNL/CDIAC-74, 1994.
- Dore, J. E., Lukas, R., Sadler, D. W., Church, M. J. and Karl, D. M.: Physical and biogeochemical modulation of ocean acidification in the central North Pacific, *Proceedings of the National Academy of Sciences*, 106, 12235-12240,
- 945 <https://doi.org/10.1073/pnas.0906044106>, 2009.
- D’Ortenzio, F., Antoine, D. and Marullo, S.: Satellite-driven modeling of the upper ocean mixed layer and air–sea CO<sub>2</sub> flux in the Mediterranean Sea, *Deep Sea Research*, 55 (4), 405-434, <https://doi.org/10.1016/j.dsr.2007.12.008>, 2008.
- Feely, R. A., Doney, S. C. and Cooley, S. R.: Ocean Acidification: Present conditions and future changes in a high-CO<sub>2</sub> world, *Oceanography*, 22(4), 36-47, 2009.
- 950 Frayse, M., Pinazo, C., Faure, V. M., Fuchs, R., Lazzari, P., Raimbault, P. and Peyraud, I.: Development of a 3D Coupled Physical-Biogeochemical Model for the Marseille Coastal Area (NW Mediterranean Sea): What Complexity Is Required in the Coastal Zone? *PLoS ONE*, 8(12): e80012, <https://doi.org/10.1371/journal.pone.0080012>, 2013.
- Frayse, M., Pairaud, I., Ross, O. N., Faure, V. M. and Pinazo, C.: Intrusion of Rhone River diluted water into the Bay of Marseille: Generation processes and impacts on ecosystem functioning, *Journal of Geophysical Research: Oceans*, 119,
- 955 <https://doi.org/10.1002/2014JC010022>, 2014.
- Friedlingstein, P., Jones, M. W., O’Sullivan, M., Andrew, R. M., Bakker, D. C. E., Hauck, J., Le Quéré, C., Peters, G. P., Peters, W., Pongratz, J., Sitch, S., Canadell, J. G., Ciais, P., Jackson, R. B., Alin, S. R., Anthoni, P., Bates, N. R., Becker, M., Bellouin, N., Bopp, L., Chau, T. T. T., Chevallier, F., Chini, L. P., Cronin, M., Currie, K. I., Decharme, B., Djeutchouang, L. M., Dou, X., Evans, W., Feely, R. A., Feng, L., Gasser, T., Gilfillan, D., Gkritzalis, T., Grassi, G., Gregor,
- 960 L., Gruber, N., Gurses, O., Harris, I., Houghton, R. A., Hurtt, G. C., Iida, Y., Ilyina, T., Lujikx, I. T., Jain, A., Jones, S. D., Kato, E., Kennedy, D., Klein Goldewijk, K., Knauer, J., Korsbakken, J. I., Körtzinger, A., Landschützer, P., Lauvset, S. K., Lefèvre, N., Lienert, S., Liu, J., Marland, G., McGuire, P. C., Melton, J. R., Munro, D. R., Nabel, J. E. M. S., Nakaoka, S.-I., Niwa, Y., Ono, T., Pierrot, D., Poulter, B., Rehder, G., Resplandy, L., Robertson, E., Rödenbeck, C., Rosan, T. M., Schwinger, J., Schwingshackl, C., Séférian, R., Sutton, A. J., Sweeney, C., Tanhua, T., Tans, P. P., Tian, H., Tilbrook, B., Tubiello, F., van der Werf, G. R., Vuichard, N., Wada, C., Wanninkhof, R., Watson, A. J., Willis, D., Wiltshire, A. J., Yuan, W., Yue, C., Yue, X., Zaehle, S. and Zeng, J.: Global Carbon Budget 2021, *Earth System Science Data*, 14, 1917-2005, <https://doi.org/10.5194/essd-14-1917-2022>, 2022.

- Gatti, J., Petrenko, A., Devenon, J. -L., Leredde, Y. and Ulses, C.: The Rhone River dilution zone present in the northeastern shelf of the Gulf of Lion in December 2003, *Continental Shelf Research*, 26, 1794-1815, <https://doi.org/10.1016/j.csr.2006.05.012>, 2006.
- Gattuso, J. -P., Frankignoulle, M. and Wollast, R.: Carbon and carbonate metabolism in coastal aquatic ecosystems, *Annual Review of Ecology, Evolution, and Systematics*, 29, 405–34, <https://doi.org/10.1146/annurev.ecolsys.29.1.405>, 1998.
- Gonzales-Dávila, M., Santana-Casiano, J. M., Rueda, M. J. and Llinás, O.: The water column distribution of carbonate system variables at the ESTOC site from 1995 to 2004, *Biogeosciences*, 7, 3067-3081, <https://doi.org/10.5194/bg-7-3067-2010>, 2010.
- Guerzoni, S., Molinaroli, E. and Chester, R.: Saharan dust inputs to the western Mediterranean Sea: depositional patterns, geochemistry and sedimentological implications, *Deep Sea Research Part II: Topical Studies in Oceanography*, 44(3-4), 631-654, [https://doi.org/10.1016/S0967-0645\(96\)00096-3](https://doi.org/10.1016/S0967-0645(96)00096-3), 1997.
- Gustafsson, E., Wällstedt, T., Humborg, C., Mörth, C. -M. and Gustafsson, B. G.: External total alkalinity loads versus internal generation: The influence of nonriverine alkalinity sources in the Baltic Sea, *Global Biogeochemical Cycles*, 28, 1358–1370, <https://doi.org/10.1002/2014GB004888>, 2014.
- Hassoun, A. E. R., Gemayel, E., Krasakopoulou, E., Goyet, C., Abboud-Abi Saab, M., Ziveri, P., Touratier, F., Guglielmi, V. and Flaco, C.: Modeling of the Total Alkalinity and the Total Inorganic Carbon in the Mediterranean Sea, *Journal of Water Resources and Ocean Science*, 4(1), 24-32, <https://doi.org/10.11648/j.wros.20150401.14>, 2015.
- Hopkins, T. S.: The structure of Ionian and Levantine Seas, *Rep. Meteorol. Oceanogr.*, 41(II), pp. 35 – 56, Harvard Univ., Cambridge, Mass, 1992.
- Ingrosso, G., Giani, M., Cibic, T., Karuza, A., Kralj, M. and Del Negro, P.: Carbonate chemistry dynamics and biological processes along a river–sea gradient (Gulf of Trieste, northern Adriatic Sea), *Journal of Marine Systems*, 155, 35-49, <https://doi.org/10.1016/j.jmarsys.2015.10.013>, 2016.
- Kapsenberg, L., Alliouane, S., Gazeau, F., Mousseau, L. and Gattuso, J. -P.: Concomitant Ocean acidification and increasing total alkalinity at a coastal site in the NW Mediterranean Sea (2007-2015), *Ocean Science*, 13, 411-426, <https://doi.org/10.5194/os-13-411-2017>, 2017.
- Krumins, V., Gehlen, M., Arndt, S., Van Cappellen, P. and Regnier, P.: Dissolved inorganic carbon and alkalinity fluxes from coastal marine sediments: Model estimates for different shelf environments and sensitivity to global change, *Biogeosciences*, 10, 371–398, <https://doi.org/10.5194/bg-10-371-2013>, 2013.
- [Kwiatkowski, L. and Orr, J. C.: Diverging seasonal extremes for ocean acidification during the twenty-first century, \*Nature Climate Change\*, 8\(2\), 141-145, https://doi.org/10.1038/s41558-017-0054-0, 2018.](https://doi.org/10.1038/s41558-017-0054-0)
- Lajaunie-Salla, K., Diaz, F., Wimart-Rousseau, C., Wagener, T., Lefevre, D., Yohia, C., Xueref-Remy, I., Nathan, B., Armengaud, A., and Pinazo, C.: Implementation and assessment of a carbonate system model (Eco3m-CarbOx v1.1) in a highly dynamic Mediterranean coastal site (Bay of Marseille, France), *Geoscience Model Development*, 14, 295–321, <https://doi.org/10.5194/gmd-14-295-2021>, 2021.

- Laruelle, G. G., Dürr, H. H., Slomp, C. P. and Borges, A. V.: Evaluation of sinks and sources of CO<sub>2</sub> in the global coastal ocean using a spatially explicit typology of estuaries and continental shelves, *Geophysical Research Letters*, 37, L15607, <https://doi.org/10.1029/2010GL043691>, 2010.
- 1005 Laruelle, G. G., Lauerwald, R., Pfeil, B. and Regnier, P.: Regionalized global budget of the CO<sub>2</sub> exchange at the air-water interface in continental shelf seas, *Global Biogeochemical Cycles*, 28-11, 1199-1214, <https://doi.org/10.1002/2014GB004832>, 2014.
- Lewis, E. and Wallace, D. W. R.: Program developed for CO<sub>2</sub> system calculations, 1998.
- Lovenduski, N. S., Gruber, N., Scott, C. D. and Lima, I. D.: Enhanced CO<sub>2</sub> outgassing in the Southern Ocean from a positive phase of the Southern Annular Mode, *Global Biogeochemical Cycles*, 21, <https://doi.org/10.1029/2006GB002900>, 2007.
- 1010 Luchetta, A., Cantoni, C. and Catalano, G.: New observations of CO<sub>2</sub>-induced acidification in the northern Adriatic Sea over the last quarter century. *Chemistry and Ecology*, 26, 1-17, <https://doi.org/10.1080/02757541003627688>, 2010.
- Ludwig, W. E., Dumont, M., Meybeck, M. and Heussner, S.: River discharges of water and nutrients to the Mediterranean and Black Sea: Major drivers for ecosystem changes during past and future decades? *Progress in Oceanography*, 80(3-4), 199–217, <https://doi.org/10.1016/j.pocean.2009.02.001>, 2009.
- 1015 Lueker, T. J., Dickson, A. G. and Keeling, C. D.: Ocean pCO<sub>2</sub> calculated from dissolved inorganic carbon, alkalinity, and equations for K<sub>1</sub> and K<sub>2</sub>: Validation based on laboratory measurements of CO<sub>2</sub> in gas and seawater at equilibrium, *Marine Chemistry*, 70, 105–119, [https://doi.org/10.1016/S0304-4203\(00\)00022-0](https://doi.org/10.1016/S0304-4203(00)00022-0), 2000.
- Maréchal, D.: A soil-based approach to rainfall-runoff modelling in ungauged catchments for England and Wales, Ph.D. Thesis, Cranfield University, 157pp, 2004.
- 1020 Middelburg, J. J.: *Marine carbon biogeochemistry, A primer for earth system scientists*, Springer Briefs in Earth System Sciences, Springer Nature Switzerland AG, Cham, Switzerland, 2019.
- Middelburg, J. J., Soetaert, K. and Hagens, M.: Ocean alkalinity buffering and biogeochemical processes, *Reviews of Geophysics*, 58 (3), e2019RG000681, <https://doi.org/10.1029/2019RG000681>, 2020.
- 1025 Millet, B., Pinazo, C., Banaru, D., Pagès, R., Guiart, P. and Pairaud, I.: Unexpected spatial impact of treatment plant discharges induced by episodic hydrodynamic events: Modelling lagrangian transport of fine particles by Northern Current intrusions in the Bays of Marseille (France), Édité par João Miguel Dias, *PLoS ONE*, 13 (4), <https://doi.org/10.1371/journal.pone.0195257>, 2018.
- Millero, F. J.: Thermodynamics of the carbon dioxide system in the oceans, *Geochimica Cosmochimica Acta*, 59, 661–677, [https://doi.org/10.1016/0016-7037\(94\)00354-O](https://doi.org/10.1016/0016-7037(94)00354-O), 1995.
- 1030 Millot, C.: The Golf of Lions' hydrodynamic, *Continental Shelf Research*, 10, 885-894, 1990.
- Morel, A. and André, J. -M.: Pigment distribution and primary production in the western Mediterranean as derived and modelled from coastal zone colour scanner observations, *96(C7)*, 12685-12698, <https://doi.org/10.1029/91JC00788>, 1991.
- Morris, A. W. and Riley, J. P.: The bromide/chlorinity and sulphate/ chlorinity ratio in sea water, *Deep-Sea Research*, 13, 699-705, 1966.
- 1035

- Mucci, A.: The solubility of calcite and aragonite in seawater at various salinities, temperatures, and one atmosphere total pressure, *American Journal of Science*, 283, 780–799, <https://doi.org/10.2475/ajs.283.7.780>, 1983.
- Orr, J. C., Fabry, V. J., Aumont, O., Bopp, L., Doney, S. C., Feely, R. A., Gnanadesikan, A., Gruber, N., Ishida, A. and Joos, F.: Anthropogenic Ocean acidification over the twenty-first century and its impact on calcifying organisms, *Nature*, 437(7059), 681–686, <https://doi.org/10.1038/nature04095>, 2005.
- 1040 Pairaud, I., Gatti, J., Bensoussan, N., Verney, R., and Garreau, P.: Hydrology and circulation in a coastal area off Marseille: Validation of a nested 3D model with observations, *J. Marine Syst.*, 88, 20–33, <https://doi.org/10.1016/j.jmarsys.2011.02.010>, 2011.
- Pont, D., Simonnet, J.-P., and Walter, A. V.: Medium-term changes in suspended sediment delivery to the Ocean: Consequences of catchment heterogeneity and river management (Rhône River, France), *Estuarine, Coastal and Shelf Science*, 54, 1–18, <https://doi.org/10.1006/ecss.2001.0829>, 2002.
- 1045 Pujo-Pay, M., Conan, P., Joux, F., Oriol, L., Naudin, J. -J. and Cauwet, G.: Impact of phytoplankton and bacterial production on nutrient and DOM uptake in the Rhône River plume (NW Mediterranean), *Marine Ecology Progress Series*, 315, 43–54, <https://doi.org/10.3354/meps315043>, 2006.
- 1050 Radach, G. and Moll, A.: Review of three-dimensional ecological modelling related to the North Sea shelf system. Part II: model validation and data needs, *Oceanography and Marine Biology*, 44, 1–60, 2006.
- Revelante, N. and Gilmartin, M.: The effect of Po River discharge on phytoplankton dynamics in the Northern Adriatic Sea, *Marine Biology*, 34, 259–271, <https://doi.org/10.1007/BF00388803>, 1976.
- Riley, J. P.: The occurrence of anomalously high fluoride concentrations in the North Atlantic, *Deep-Sea Research* 12, 219–220, 1965.
- 1055 Riley, J. P. and Tongudai, M.: The major cation/chlorinity ratios in sea water, *Chemical Geology*, 2, 263–269, 1967.
- Roobaert, A., Laruelle, G. G., Landschützer, P., Gruber, N., Chou, L. and Regnier, P.: The Spatiotemporal Dynamics of the Sources and Sinks of CO<sub>2</sub> in the Global Coastal Ocean, *Global Biogeochemical Cycles*, 33, 1693–1714, <https://doi.org/10.1029/2019GB006239>, 2019.
- 1060 Ross, O. N., Frayse, M., Pinazo, C. and Pairaud, I.: Impact of an intrusion by the Northern Current on the biogeochemistry in the Eastern Gulf of Lion, NW Mediterranean, *Estuarine, Coastal and Shelf Science*, 170, 1–9, 2016.
- Salat, J., Garcia, M. A., Cruzado, A., Palanques, A., Arin, L., Gomis, D., Guillen, J., De Leon, A., Puigdefàbregas, J., Sospedra, J. and Velasquez, Z. R.: Seasonal changes of water mass structure and shelf slope exchanges at the Ebro Shelf (NW Mediterranean), *Continental Shelf Research*, 22, pp. 327–348, [https://doi.org/10.1016/S0278-4343\(01\)00031-0](https://doi.org/10.1016/S0278-4343(01)00031-0), 2002.
- 1065 Schaeffer, A., Molcard, A., Forget, P., Fraunié, P. and Garreau, P.: Generation mechanisms for mesoscale eddies in the Gulf of Lions: radar observation and modelling, *Ocean Dynamics*, 61, 1587–1609, <https://doi.org/10.1007/s10236-011-0482-8>, 2011.
- Schneider, A., Douglas, W. R. W. and Körtzinger, A.: Alkalinity of the Mediterranean Sea, *Geophysical Research Letters*, 34, <https://doi.org/10.1029/2006GL028842>, 2007.

- 1070 Sempere, R., Charrière, B., Van Wambeke, F. and Cauwet, G.: Carbon inputs of the Rhône River to the Mediterranean Sea: Biogeochemical implications, *Global Biogeochemical Cycles*, American Geophysical Union, 14(2), 669-681, <https://doi.org/10.1029/1999GB900069>, 2000.
- Sharp, J. D., Pierrot, D., Humpbreys, M. P., Epitalon, J. -M., Orr, J. C., Lewis, E. R. and Wallace, D. W. R.: CO2SYSv3 for MATLAB (v3.0.1). Zenodo [code] <https://doi.org/10.5281/zenodo.3952803>, 2020.
- 1075 *Stow, C. A., Jolliff, J., McGillicuddy Jr, D. J., Doney, S. C., Allen, J. I., Friedrichs, M. A., Rose, K. A. and Wallhead, P.: Skill assessment for coupled biological/physical models of marine systems, Journal of Marine Systems, 76(1-2), 4-15, https://doi.org/10.1016/j.jmarsys.2008.03.011, 2009.*
- Thomas, H., Bozec, Y., Elkalay, K. and De Baar, H. J. W.: Enhanced Open Ocean Storage of CO<sub>2</sub> from Shelf Sea Pumping, *Science*, 304-5673, 1005-1008, <https://doi.org/10.1126/science.1095491>, 2004.
- 1080 Turi, G., Lachkar, Z. and Gruber, N.: Spatiotemporal variability and drivers of pCO<sub>2</sub> and air-sea CO<sub>2</sub> fluxes in the California Current System: an eddy-resolving modeling study, *Biogeosciences*, 11, 671-690, <https://doi.org/10.5194/bg-11-671-2014>, 2014.
- Uppstrom, L. R.: The boron/chlorinity ratio of deep-sea water from the Pacific Ocean, *Deep-Sea Research*, 21, 161-162, 1974.
- 1085 Urbini, L., Inghrosso, G., Djakovac, T., Piacentino, S. and Giani, M.: Temporal and Spatial Variability of the CO<sub>2</sub> System in a Riverine Influenced Area of the Mediterranean Sea, the Northern Adriatic, *Frontiers in Marine Science*, 7-679, <https://doi.org/10.3389/fmars.2020.00679>, 2020.
- Van Slyke, D. D.: On the measurement of buffer values and on the relationship of buffer value to the dissociation constant of the buffer and the concentration and reaction of the buffer solution, *Journal of Biological Chemistry*, 52, 525-570, 1922.
- 1090 Wanninkhof, R.: Relationship between wind speed and gas exchange over the ocean revisited, *Limnology and Oceanography: Methods*, 12 (6), 351-362, <https://doi.org/10.4319/lom.2014.12.351>, 2014.
- Weiss, R. F.: Carbon dioxide in water and seawater: The solubility of a non-ideal gas, *Marine Chemistry*, 2(3), 203-215, [https://doi.org/10.1016/0304-4203\(74\)90015-2](https://doi.org/10.1016/0304-4203(74)90015-2), 1994.
- Wimart-Rousseau, C., Lajaunie-Salla, K., Marrec, P., Wagener, T., Raimbault, P., Lagadec, V., Lafont, M., Garcia, N., Diaz, F., Pinazo, C., Yohia, C., Garcia, F., Xueref-Remy, I., Blanc, P. E., Armengaud, A., and Lefèvre, D.: Temporal variability of the carbonate system and air-sea CO<sub>2</sub> exchanges in a Mediterranean human-impacted coastal site, *Estuar. Coast. Shelf S.*, 236, <https://doi.org/10.1016/j.ecss.2020.106641>, 2020.
- 1095 Wolf-Gladrow, D. A., Zeebe, R. E., Klaas, C., Körtzinger, A. and Dickson, A. G.: Total Alkalinity: The explicit conservative expression and its application to biogeochemical processes, *Marine Chemistry*, 106, 287-300, <https://doi.org/10.1016/j.marchem.2007.01.006>, 2007.
- 1100 Yohia, C.: Genèse du mistral par interaction barocline et advection du tourbillon potentiel, *Climatologie*, 13, 24-37, <https://doi.org/10.4267/climatologie.1182>, 2017.

a mis en forme : Non souligné, Couleur de police : Automatique

Code de champ modifié